THE JOURNAL OF PHYSICAL CHEMISTRY C
A JOURNAL OF THE AMERICAN CHEMICAL SOCIETY

pubs.acs.org/JPCC

Article

Understanding the Evolution of the Structure and Electrical Properties during Crystallization of $Li_{1.5}Al_{0.5}Ge_{1.5}(PO_4)_3$ and $Li_{1.5}Sc_{0.17}Al_{0.33}Ge_{1.5}(PO_4)_3$ NASICON -Type Glass Ceramics

Jeferson A. Dias,* Silvia H. Santagneli,* Ana C. M. Rodrigues, Naiza V. Bôas, and Younès Messaddeq

Cite This: *J. Phys. Chem. C* 2023, 127, 6207−6225

Read Online

ACCESS | Metrics & More | Article Recommendations | Supporting Information

ABSTRACT: In this paper, the effects of crystallization advance on the material structure and electrical properties of lithium-ion Na^+ super ionic conductor (NASICON) glass ceramics were investigated. Glasses with $Li_{1.5}Al_{0.5}Ge_{1.5}(PO_4)_3$ and $Li_{1.5}Sc_{0.17}Al_{0.33}Ge_{1.5}(PO_4)_3$ compositions were crystallized in controlled conditions to obtain gradual increment of the volume crystallized fraction. The glass-to-crystal transformation was then monitored by differential scanning calorimetry analysis (DSC), X-ray diffractometry (XRD), Raman spectroscopy, solid-state nuclear magnetic resonance spectroscopy (MAS NMR), and electron microscopy, along with chemical analyses. Finally, the electrical properties of the specimens were evaluated by impedance spectroscopy to observe the changes in electrical properties according to the crystallization advance. Results revealed that glasses containing scandium are more stable against crystallization than their neat counterparts. Crystallization led to the formation of single-phase NASICON glass ceramics. Scandium induced a lattice expansion of the NASICON structure. Furthermore, crystallization induces remarkable structural changes in the materials as a whole, either in local order or in medium to long order. No important increase in conductivity was observed in earlier stages of crystallization. After the percolation of crystals, conductivity increases sharply and the remaining glassy phase has little impact on the total conductivity of the material. Scandium expands the rhombohedral structure but increases the glass stability and reduces the sizes of crystals for the fully crystallized glass ceramics. Glass ceramics with larger grains are more propitious for conductivity than the more refined ones. Therefore, this paper offers key information about the understanding of NASICON crystallization and its structural evolution, providing important insights into the crystallization of these electrolytes.

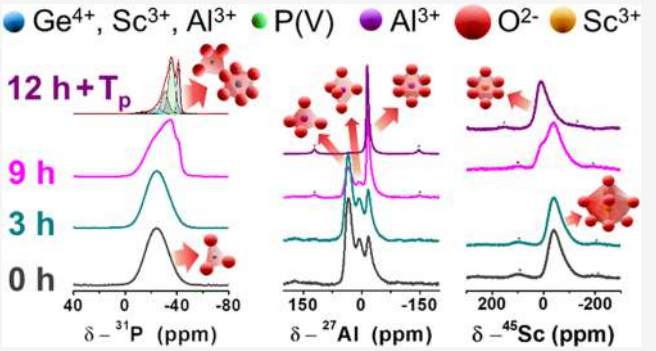

1. INTRODUCTION

The production of stable and highly conductive solid-state electrolytes is a challenge for upcoming technologies such as grid energy storage and electrical vehicles.[1−3] Solid-state electrolytes are alternatives for the liquid and gel ones, which are usually flammable and easily lost during application.[3] In the search for good candidates for solid-state electrolytes, Na^+ super ionic conductor (NASICON) compounds have been gaining ground since 1976[4] for this use.[5] They are phosphate-type compounds with the basic-$A^{(I)}B_2^{(IV)}(PO_4)_3$ stoichiometry, in which: (1) $A^{(I)}$ is a monovalent mobile cation (e.g., Li^+,[6−8] Na^+,[9−11] Ag^+ [12]) and (2) $B^{(IV)}$ an octahedrally coordinated cation, surrounded by oxygen anions (e.g., Zr^{4+},[13,14] Ti^{4+},[6,15] Ge^{4+},[16−18] Hf^{4+} [19,20]). Thus, lithium-ion NASICONs utilize Li^+ as the mobile cation in the compound's structure. They are promising candidates to be used in practically all-solid-state batteries because (1) they can present conductivity close to gel and liquid electrolytes when proper strategies of aliovalent ionic substitution and methods for preparation are used,[5,21] and (2) the stability to air moisture is better than other candidates as solid-state electrolytes, such as garnets and glass sulfides.[22,23]

Importantly, highly conductive NASICON compounds require changes in their basic composition to increase both the charge transport concentration and mobility.[24] Neat-$A^{(I)}B_2^{(IV)}(PO_4)_3$ compounds present restricted conductivity, usually at the order of 10^{-6} S cm^{-1}.[25] Thus, partial substitution of the $B^{(IV)}$ cation for trivalent ones ($B^{(III)}$) is certainly the most successful strategy to increase the charge carrier concentration and thus conductivity of these electrolytes.[25−27] The presence of trivalent cations allows the insertion of an extra quantity of lithium cations in the structure, favoring the conductivity.[24,25] Compounds with $Li_{1+x}B^{(III)}{}_xB_{2-x}{}^{(IV)}(PO_4)_3$

Received: January 20, 2023
Revised: March 14, 2023
Published: March 22, 2023

derived stoichiometry are currently the most common and successful lithium-ion NASICONs. Among the possibilities of substituents, Al^{3+} insertions in germanium-containing compounds have allowed the production of one of the highest conductive NASICON electrolytes.[25] NASICON compounds with $x \sim 0.5$ in this latter stoichiometry prototype (i.e., $Li_{1.5}Al_{0.5}Ge_{1.5}(PO_4)_3$ (LAGP)) demonstrate optimal conducting properties in this system.[28−30] Although this system is one of the most explored NASICONs in the last decades, new compositional modifications are still possible to increase its conductivity. Nikodimus et al.[16] have recently introduced a further compositional modification of $Li_{1.5}Al_{0.5}Ge_{1.5}(PO_4)_3$, proposing the partial substitution of Ge^{4+} for Al^{3+} and Sc^{3+} simultaneously. They observed that the $Li_{1.5}Sc_{0.17}Al_{0.33}Ge_{1.5}(PO_4)_3$ (LAScGP) compound into the $Li_{1.5}Sc_xAl_{0.5-x}Ge_{1.5}(PO_4)_3$ series can show improved ionic conductivity compared to the neat-$Li_{1.5}Al_{0.5}Ge_{1.5}(PO_4)_3$.

Composition is imperative but is not the single factor to be considered to produce an electrolyte. Preparation methods also impact electrical properties. Synthesis methods such as solid-state reaction[31,32] and solution-based methods of synthesis,[18,33,34] followed by traditional,[24,35] microwave,[36] and Spark Plasma sintering[37−39] have been proposed. Recently, there has been a vast body of literature on the production of NASICONs such as glass ceramics to obtain solid electrolytes.[5,16,30,40−42] The homogeneous melts provided by the preparation of the parent glass provide a high degree of compositional control.[43] Depending on heat treatment temperature, this procedure avoids the appearance of secondary phases after the NASICON crystallization that could block the lithium-ion motion.[44] Moreover, this technique is a simple strategy to produce specimens with complex shapes and with efficient microstructural control through crystallization.[42,43] Once robust setups for the parent glass preparation and further crystallization are usually not required, glass ceramic technology is a promising scale-up technique for NASICON preparation.

It is worth noting that most of the studies focus on evaluating the conductivity of the totally crystallized glass ceramic.[5,16,25] There is still a lack of knowledge about how much the electrical properties change during the glass-to-crystal transformation. An in-depth study of the local- to long-range order changes according to crystallization advance is equally important and is still needed. These insights are important as the crystallization control can be a powerful strategy to change the microstructure of the specimens to obtain improved electrical performance.[45,46]

Therefore, this paper aims to make an in-depth study of the structural and also microstructural evolution throughout the crystallization of a precursor glass in order to obtain a NASICON glass ceramic. Analyzing how much the electrical properties are impacted by the crystallization advance is also evaluated. To do this, the heat treatment parameters were controlled to obtain a systematic increment of crystals in these electrolytes. The well-studied $Li_{1.5}Al_{0.5}Ge_{1.5}(PO_4)_3$ and the recently proposed $Li_{1.5}Sc_{0.17}Al_{0.33}Ge_{1.5}(PO_4)_3$[16] compositions were used to prepare the glass ceramics due to their great melting ability and the propitious electrical performance already observed for the totally crystallized electrolytes. Thus, the structure evolution at long order was investigated in detail by X-ray diffractometry (XRD) together with Rietveld refinements, at medium to long order by Raman spectroscopy, and at local order by solid-state nuclear magnetic resonance (NMR) spectroscopy. Differential scanning calorimetry (DSC) analysis was used to monitor the advance of crystallization, together with scanning electron microscopy (SEM) and transmission electron microscopy (TEM). Selected glasses and glass ceramics had their compositions determined by energy-dispersive spectroscopy (EDS) (coupled to SEM and TEM analyses), X-ray fluorescence (XRF), and inductively coupled plasma-optical emission spectroscopy (ICP-OES). Finally, the electrical properties were recorded through impedance spectroscopy in controlled temperatures to observe the variation of conductivity and activation energy for lithium-ion motion according to the crystallization advance.

2. METHODS

In this section, the methods used for the glass ceramics preparation and their characterization are described in detail.

2.1. Glass Ceramics Preparation. The parent glasses were prepared by melting-quenching of the raw precursors. Lithium carbonate (Li_2CO_3, Riedel-de Haën, ≥99%), aluminum metaphosphate ($Al(PO_3)_3$, Alfa Aesar, ≥98.3%), scandium oxide (Sc_2O_3, Merck/Sigma-Aldrich, 99.9%), germanium oxide (GeO_2, Alfa Aesar, 99.999%), and ammonium dihydrogen phosphate ($(NH_4)H_2PO_4$, Merck/Sigma-Aldrich, ≥98%) were weighted in stoichiometric quantities to prepare glass batches of approximately 25 g. Glasses with $Li_{1.5}Al_{0.5}Ge_{1.5}(PO_4)_3$ and $Li_{1.5}Sc_{0.17}Al_{0.33}Ge_{1.5}(PO_4)_3$ nominal compositions were prepared (called in this paper LAGP and LAScGP for simplicity, respectively). The precursors were mixed in a mortar for at least 30 min and then transferred to a platinum crucible. The heat treatments of the precursor mixtures to prepare the parent glasses were carried out in an EDG FC-1 furnace under a constant heating rate of 10 °C min^{-1}. Three steps for the treatment were used, following adaptations from a previous study of our group:[47] (1) 400 °C for 2 h to decompose the ammonium dihydrogen phosphate; (2) 750 °C for 2 h to decompose the lithium carbonate to form lithium oxide; and finally, (3) 1200 °C for 30 min to melt the oxide precursors. The homogeneous melts were quickly quenched to a preheated steel mold (450 °C) and immediately inserted into a preheated furnace (also at 450 °C) for annealing. The annealing was conducted for 6 h to release the stress arising from the quenching. Importantly, preheating the molds follows the procedure used by Itkis et al.[48] We noticed that this process is imperative to prepare mechanically stable specimens. Otherwise, the glasses cracked right after being in contact with the molds and coherent monoliths were not possible to be prepared.

The glasses were cut into specimens of approximately 0.5 cm × 1.0 cm × 1.5 cm (thickness × width × length), polished through a series of tungsten carbide sandpapers (100−1000 grit), and then to alcohol soluble diamond pastes (6−0.1 μm). The optically polished specimens were submitted to heat treatment for crystallization utilizing an EDG 300 furnace coupled to an external thermocouple for better temperature control. In order to obtain partially crystallized samples (glass ceramics), the precursor glasses were submitted to single heat treatments at temperatures between their glass-transition temperature (T_g) and onset of crystallization (T_x). Therefore, the $T_g + (T_x - T_g)/3$ expression was utilized to set the temperature for crystallization, that is, closer to T_g than T_x. For the LAGP glass, it was found that the temperature of maximum nucleation rate coincides with T_g, justifying the chosen

https://doi.org/10.1021/acs.jpcc.3c00476
J. Phys. Chem. C 2023, 127, 6207−6225

conditions.[45] The total period of heat treatment for each composition was determined by gradually transforming the visually transparent glasses into totally opaque glass ceramics. Furthermore, one additional sample for each composition was submitted (1) at the maximum period of heat treatment and then to the temperature of crystallization peak (T_p), and (2) directly at the temperature of crystallization peak (T_p), both for 1 h. These additional samples were prepared to eliminate the presence of any remaining glassy phase in the specimens, making these samples useful as patterns for comparison of totally crystallized glass ceramics.

2.2. Characterization. The characteristic temperatures of two parent glasses (T_g, T_x, and T_p) were measured by DSC Netzsch STA 449 F3 Jupiter equipment for these analyses. About 20 mg samples were placed into platinum crucibles, and the analyses were carried out in the 200−800 °C interval. Continuous nitrogen flow of 100 mL min^{-1} and a heating rate of 10 °C min^{-1} were the conditions used for the experiments. To observe the changes in the thermal events and to monitor the advances in crystallization for the glass ceramics, the DSC technique was also used for the glass ceramics using the same experimental setup. However, the specimens were previously powdered to take into account any possible inhomogeneity from crystallization throughout the material's bulk.

The crystallographic characterization was performed by XRD of the powdered samples. This technique was carried out in a Rigaku Smartlab SE diffractometer. Copper anode (Cu Kα, 1.540593 Å) was used at an energy power of 1.0 kW (40 kV, 25 mA). A constant speed rate of 2° min^{-1} and a step of 0.02° were used. Rietveld refinement was performed based on XRD data for a complementary crystallographic characterization and to estimate the crystallized volume fraction (α). The crystallographic card from the Inorganic Crystal Structure Database (ICSD # 263764)[18] was utilized as the pattern for the $LiGe_2(PO_4)_3$-based NASICON structure. The GSAS-EXPGUI software[49] was employed for the refinements. A pattern of yttrium oxide (Y_2O_3, Merck/Sigma-Aldrich, 99.99%) was submitted to the XRD analyses under the same conditions from the glass and glass ceramics. Instrumental parameters for the diffractometer were then acquired by Le Bail refinement of this pattern. The software used for the Le Bail refinement was the same used for the Rietveld refinements. To properly obtain α, Rietveld refinements following the Internal Standard Method[50] were performed. The same pattern (Y_2O_3) used for the Le Bail refinement was structurally characterized to confirm that it is monophasic and that it has a cubic structure (Figure S1, data interpretation according to refs 51−57). The conditions and equipment for the structural characterization of the pattern were the same as described in this section. After that, the pattern was homogenized with the powdered samples at a proportion of 35 wt % in an agate mortar for at least 30 min. New X-ray diffractograms were recorded and analyzed following the same conditions described upward. Lastly, the crystallite sizes (D) were estimated by the Lorentzian broadening of the diffraction peaks,[58] discounting the contribution of the instrumental broadening.

Raman and multinuclear uni- and bidimensional solid-state NMR spectroscopies were utilized for the structural study of the medium- and local-order range chemical environment change, respectively, according to the advance of crystallization. The former technique was carried out in a HORIBA Jobin Yvon-HR800 spectrophotometer. The samples were powdered prior to the analysis to ensure homogeneity of crystallization and exposed to a helium−neon laser (λ = 632.8 nm) under amplification of 50×. Each spectrum was collected in the 200−1600 cm^{-1} range, with a total exposure time of 60 s and through 12 accumulations.

High-resolution solid-state magic angle spinning (MAS) NMR was performed by a Bruker Advance III 400WB HD spectrometer functioning at 9.4 T, with a triple resonance MAS NMR probe operating at a spinning speed of 14 kHz. Single-pulse ^{31}P experiments were performed at 162.0 MHz, using an excitation pulse of 3.1 s length and a recycle delay of 500 s. For ^{27}Al and ^{45}Sc nuclei, the signals were recorded at 104.3 and 97.2 MHz using a small flip-angle excitation of 1.4 and 1 μs and a recycle decay of 2 and 1 s, respectively. Two-dimensional (2D) triple quantum magic angle spinning spectra were measured using the three-pulse z-filtering variant, following the procedures from Medek et al.,[59] Amoureux et al.,[60] and a previous study by our group.[47] Furthermore, a rotor-synchronized acquisition of the indirect dimension was used with the following acquisition parameters: pulse lengths 5.4 and 1.7 μs for the first and second pulses applied with a ^{27}Al nutation frequency of 50 kHz and 10 μs for the soft detection pulse applied with a ^{27}Al nutation frequency of 14 kHz. Data are presented in the sheared mode by projecting 2D contours for each individual site onto the F1 and F2 axes. The chemical shifts of all spectra were referenced to 85% H_3PO_4, Al^{3+} solution 1 mol L^{-1}, and powdered $ScPO_4$ (−48.2 ppm)[61] for ^{31}P, ^{27}Al, and ^{45}Sc nuclei, respectively. Signal deconvolution was made using the Gaussian model for ^{31}P,[47] Czjzek model for ^{27}Al,[62,63] and ^{45}Sc were performed using the DMFIT software.[64]

$^{27}Al\{^{31}P\}$ rotational echo double resonance (REDOR) and $^{31}P\{^{27}Al\}$ rotational echo adiabatic passage double-resonance (REAPDOR) experiments were carried out based on standard setups from the literature.[65,66] To do this, the normalized signal differences ($\Delta S/S_0$) were plotted against the dipolar evolution time (NT_r). Optimum π pulse lengths for the decoupling channel were set by maximizing the REDOR difference signal ΔS at a chosen dephasing time. The π-pulse lengths of ^{31}P and ^{27}Al were 6.5 and 5.2 μs, respectively. In the REDOR experiments, phase cycling according to the XY4 scheme was used for the ^{31}P recoupling pulses. Normalized difference signal intensities $\Delta S/S_0$ (corresponding to the signal amplitudes without (S_0) and with (S) ^{31}P pulsed irradiation) were plotted as a function of dipolar evolution time NT_r, and second moment values M_2 were extracted from the parabolic fits to the initial decay regime ($0 \leq \Delta S/S_0 \leq 0.2$). $^{31}P\{^{27}Al\}$ REAPDOR NMR experiments employing $\pi/2$ pulses for ^{31}P of 6.5 μs length and ^{27}Al adiabatic pulses of 23.8 μs length. The experiments were conducted at a ^{27}Al nutation frequency of 60 kHz measured on a liquid sample. For an analysis of the resulting REAPDOR curves, the simulation package SIMPSON[67] was used to estimate the average numbers of P−O−Al linkages for each resolved ^{31}P resonance.

The morphology of the crystals formed in the crystallization was observed through a JEOL JSM 7500F field emission gun scanning electron microscope (FEG-SEM). The cracked samples were coated with carbon before analysis. Images were collected at an accelerating voltage of 2 kV. Magnifications varied from 500 times to 25,000 times depending on the crystal's sizes for each sample. EDS was used to assess the elemental distribution in the glassy phase and crystals and to evaluate the presence of any possible

https://doi.org/10.1021/acs.jpcc.3c00476
J. Phys. Chem. C 2023, 127, 6207−6225

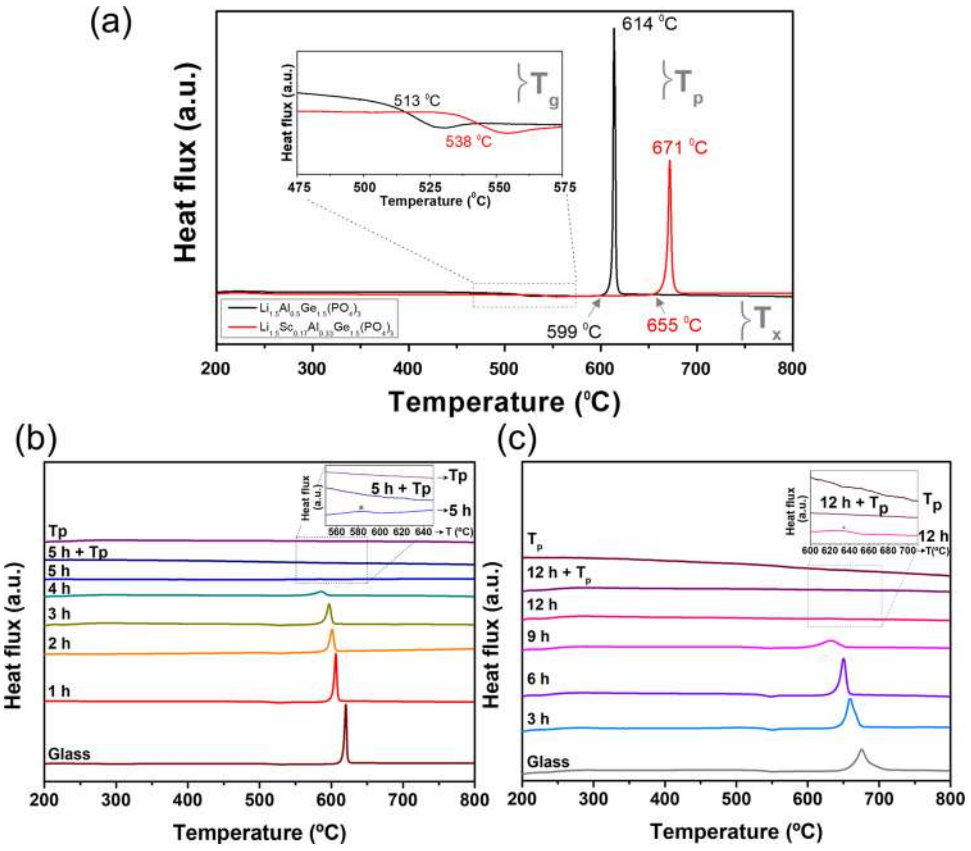

Figure 1. DSC curves for $Li_{1.5}Al_{0.5}Ge_{1.5}(PO_4)_3$ and $Li_{1.5}Sc_{0.17}Al_{0.33}Ge_{1.5}(PO_4)_3$ parent glasses and glass ceramics: (a) DSC profiles and characteristic temperatures for the parent glasses (monoliths). (b) DSC profiles for the powdered LAGP glass ceramics prepared at 542 °C for different periods of time, along with 542 °C for 5 h followed by T_p (614 °C, 1 h) and directly treated at T_p (614 °C, 1 h). (c) DSC profiles for the powdered LAScGP glass ceramics prepared at 577 °C for different periods of time, along with 577 °C for 12 h followed by T_p (671 °C, 1 h) and directly treated at T_p (671 °C, 1 h).

contaminant. This technique was performed in the same microscope but at an accelerating voltage of 10 kV. Furthermore, TEM analyses were performed in a JEOL JEM-2100Plus LaB6 200 kV microscope. For that, the glass ceramics were powdered in an agate mortar for at least 30 min. A mass of 10 mg of the resulting powder was dispersed in 1 mL of isopropyl alcohol and sonicated at 40 kHz for 30 min. Then, 20 μL of supernatant of each suspension was rapidly dripped on a formvar/carbon-supported copper grid. EDS mappings were recorded for these samples in the same equipment.

For a more complete chemical analysis, X-ray fluorescence (XRF) was performed in a Rh anode Shimadzu EDX-720 Ray ny equipment. Each powdered sample was placed in a sample port with a diameter of 2.5 cm in a quantity enough to cover the analyzing area. A radiation collimator of 1 cm was used. Semiquantitative analyses were made by fixing the Al, Ge, Sc, and P Kα signals. Further, the lithium content in the glass ceramics was determined by ICP-OES. The analyses were carried out in a Thermo, iCAP 6000 spectrophotometer. A mass of each powder was dissolved in a mixture of nitric acid (20% v/v) and hydrofluoric acid (80% v/v) in a proper Teflon flask. The suspensions were exposed to microwave radiation in a CEM MarsXpress equipment up to a complete sample dissolution. The dissolved sample was then mixed with a boric acid solution (4.5% w/v) in quantity enough to consume the excess of hydrofluoric acid, neutralized, and then diluted with Milli-Q water. The Li signals in the resulting solution were then analyzed in triplicate by ICP-OES, and the contents of this element were estimated based on calibration curves previously constructed.

Finally, the electrical properties were evaluated by impedance spectroscopy. A Solartron SI 1260 impedance meter coupled to a Solartron 1296 dielectric interface was used. Analyses were made in the frequency range of 1 MHz to 100 mHz and under an amplitude of 300 mV. Gold electrodes were deposited on the parallel opposite faces of the samples by sputtering. Analyses were made at different temperatures, from room temperature (controlled at 30 °C for all of the samples) up to 300 °C. A high-precision Novocontrol furnace with a resolution of ±0.1 °C was used for these analyses.

The ionic conductivity (σ) in a solid electrolyte is a thermally activated process. Thus, the measurements of the conductivity versus temperature allowed the obtention of the activation energy for lithium-ion motion (E_a). This estimation can be made by using an Arrhenius-type relation shown in eq 1[68]

$$\sigma = \left(\frac{\sigma_0}{T}\right) \exp\left(\frac{-E_a}{k_B T}\right) \quad (1)$$

where σ is the ionic conductivity measured at a specific temperature T and k_B is the Boltzmann constant. The parameter σ_0 is a preexponential factor that can be obtained by linearization of eq 1. Therefore, after knowing the conductivity for each temperature, the linearization of eq 1 allows the estimation of E_a.

https://doi.org/10.1021/acs.jpcc.3c00476
J. Phys. Chem. C 2023, 127, 6207−6225

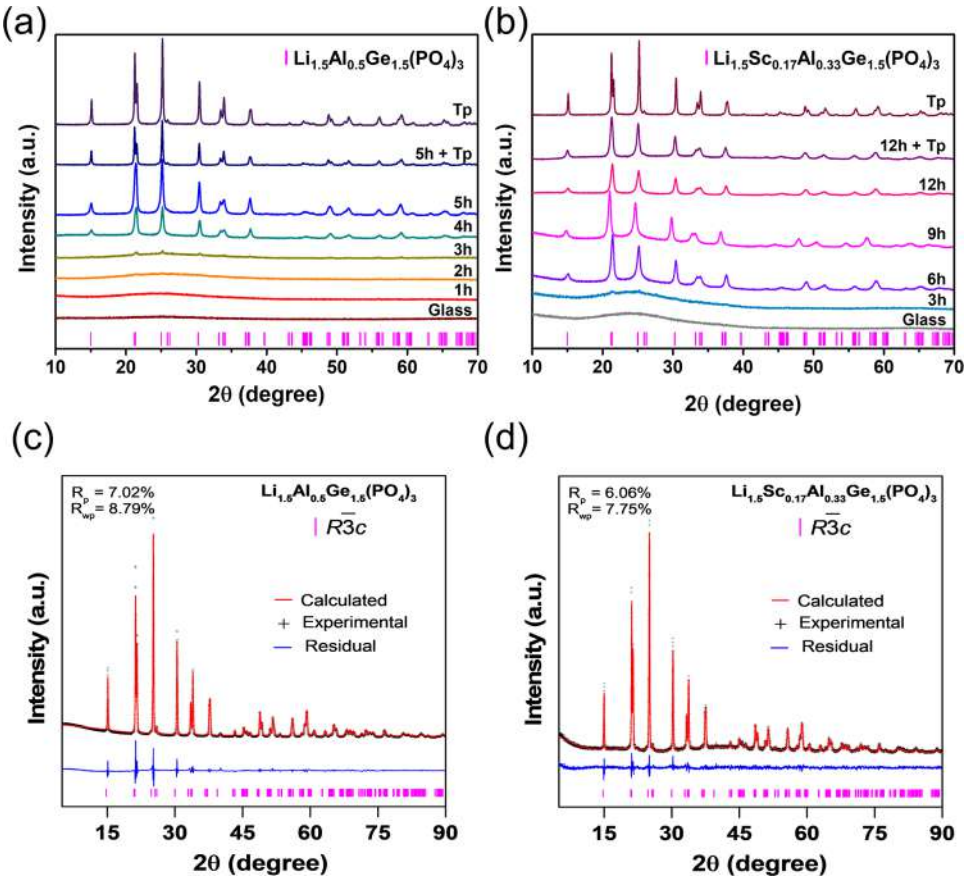

Figure 2. Crystallographic characterization of glass ceramics: (a) XRD diffractograms for LAGP glass ceramics according to the heat treatment period, along with the patterns of samples totally crystallized. (b) XRD diffractograms for LAScGP glass ceramics according to the heat treatment period, along with the patterns of samples totally crystallized. (c) Graphical results of the Rietveld refinement for the glass ceramic with LAGP composition directly heat-treated at T_p/1 h. (d) Graphical results of the Rietveld refinement for the glass ceramic with LAScGP composition directly heat-treated at T_p/1 h.

3. RESULTS AND DISCUSSION

In this section, results for the characterization of the glasses used to tailor the heat treatment conditions, the structural characterization from long-to-local range order, the microstructural characterization, and the study of electrical properties according to the heat treatments will be presented in detail.

3.1. Crystallization of Glass Ceramics. DSC analyses of the glasses were performed prior to the crystallization to properly tailor the temperatures to be used for the heat treatments for each composition. The results are shown in Figure 1. Figure 1a shows that a single and sharp crystallization peak appears for both compositions under evaluation. The characteristic temperatures T_g and T_x changed according to the composition of the NASICON parent glass. The presence of Sc^{3+} in the glasses increased both T_g and T_x compared to neat-NASICON and increased the difference between them. This indicates greater thermal stability of the glassy phase when scandium is used as an additional substituent for germanium. That is, the interval of $T_x - T_g$ was 86 °C for LAGP parent glasses, while this value increased to 117 °C for LAScGP parent glasses. The increment in the glass thermal stability can be attributed to the use of a substituent with higher polarizability than aluminum. High-polarizable cations usually promote loss of symmetry for the electrostatic field forces and hinder the cells' organization during the crystal formation, which increases the stability of the glassy phase.[69,70] Importantly, increasing the glass stability is expected to affect the crystallization kinetics of the specimens. Glass ceramics from LAGP series were prepared at 542 °C, while the specimens with LAScGP composition were at 577 °C. Even submitted to a heat treatment temperature chosen by the same rule, glasses containing scandium became totally crystallized only for periods of heat treatment much greater than the samples without this element (approximately 12 versus 5 h). This observation proposes a slower crystallization kinetic and was considered to set the total period for crystallization of each composition.

The increment of time in which the specimens were submitted to heat treatment reduced the intensity of the crystallization peak on the DSC profiles (Figure 1b,c). This result is evidently attributed to the gradual increment of crystal content in the samples and consequent reduction of the remaining glassy phase. Importantly, even the glass ceramics produced for long periods of time (5 h for LAGP and 12 h for LAScGP systems) show small crystallization peaks in the DSC profiles as observed in the insets of Figure 1b,c. These results indicate that a small content of the glassy phase remains even under these conditions. Thus, the two additional samples prepared to be used as the patterns of samples crystallized for each composition studied demonstrated no presence of crystallization peak even under amplification in these profiles, indicating total crystallization of the glassy phase. Interestingly, a left shift is seen for the DSC profiles even for short periods of

https://doi.org/10.1021/acs.jpcc.3c00476
J. Phys. Chem. C 2023, 127, 6207−6225

heat treatment. This demonstrates that a considerable quantity of nuclei and low-size crystals were formed for such conditions. That is, the crystallization was favored afterward when submitted to DSC analyses, displacing the crystallization peaks to lower temperatures than their parent glasses. Increasing the time of heat treatment, the peaks are reduced in intensity and shifts to lower temperatures, showing evidence of a progressive increment of crystals. Using a single-step heat treatment at temperatures lower than that of the crystallization peak to avoid rapid crystal growth allowed the obtention of a gradual content of crystals in the specimens. However, this process requires relatively long periods of heat treatment for a complete crystallization,[71] requiring the additional samples additionally treated at T_p as patterns for samples totally crystallized. These patterns did not show any evidence of the remaining glassy phase as already discussed, which will be confirmed later by other characterization techniques.

3.2. Structural Characterization: Monitoring the Structural Evolution from Long-to-Local Range Order. XRD was employed to evaluate the structure of the materials in a long range, that is, to check the crystalline phases formed and to confirm the formation of the NASICON phase in the glass ceramics. The diffractograms are shown in Figure 2. All of the peaks were indexed to the NASICON with $Li_{1+x}Al_xGe_{2-x}(PO_4)_3$-based structure ($R\bar{3}c$ space group, ICSD # 263764[18] related to the rhombohedral $Li_{1.48}Al_{0.48}Ge_{1.52}(PO_4)_3$ compound) either for the samples partially crystallized or for samples totally crystallized, regardless of the composition used. The parent glasses for both compositions (Figure 2a,b) demonstrated only the characteristic amorphous halo from the glasses. Thus, no evidence that prior crystallization for the glasses during the melting-quenching process has occurred.

Importantly, the precursor aluminum metaphosphate was used as an aluminum source instead of alumina (Al_2O_3) typically used to prepare glasses in these systems. This strategy was devised to reduce the melting temperature of the precursor oxide mixture. Several reports from the literature produce LAGP with temperatures higher than 1300 °C[40,47,48,72−75] due to the presence of aluminum precursors with a high melting point. The substitution of alumina into aluminum metaphosphate allowed the production of the melts with adequate viscosity for the quenching at 1200 °C and during short periods of time (~30 min) either for batches containing Sc_2O_3 or not. This result is important as long periods of time at high temperatures lead to partial lithium loss and consequent deviation from the planned stoichiometry.[5,76,77] Even though Li_2O is a thermodynamically stable compound compared to several other lithium compounds,[78] some contents could vaporize when in a multicomponent liquid phase at high temperatures. The impoverishment in lithium ions would result in secondary phases generated during NASICON crystallization,[77] losing reproducibility and also being detrimental to electrical properties.[5] Nevertheless, the absence of XRD peaks prior to the heat treatments demonstrates that the melts were efficiently produced without traces of remaining solid precursors even though the process occurred at moderate temperatures. The change of the aluminum precursor was, therefore, a simple strategy to attain melting in lower temperatures and a simple strategy to prevent lithium loss.

To confirm that lithium remained in the samples, first, there is evidence from the NASICON phases formed. Once the NASICON compounds from the LAGP-derived system have a determined stoichiometry such as $Li_{1+x}B^{(III)}{}_xB_{2-x}{}^{(IV)}(PO_4)_3$ (in our case, $B^{(III)}$ is Al^{3+} and Sc^{3+}, and $B^{(IV)}$ is Ge^{4+}), if the lithium loss was intense the NASICON phase would not properly form. That is, a series of secondary phases would be generated instead. On the other hand, our results demonstrate that single-NASICON phases were formed either containing scandium or not (Figure 2). Therefore, it is more likely that the lithium loss was small due to the strategies already discussed to prepare the glasses. In order to confirm these inferences, ICP-OES was employed for glasses and glass ceramics prepared at the highest periods of heat treatment for each composition. The numerical results are displayed in Table S1. Importantly, all of the average values are close to ones predicted by the compounds' stoichiometries (2.1−2.7 wt %, near 2.49 wt % for LAGP and 2.47 wt % for LAScGP). Therefore, an intense lithium loss was successfully avoided by tailoring the precursor sources to attain lower melting temperatures and reducing the period to melt the oxide mixture.

The increment of time used for the heat treatment gradually increased the intensity of the diffraction peaks, while the amorphous halo gradually disappeared. Notably, small peaks can be observed after 2 h for the LAGP series and after 3 h for the LAScGP one. This result confirms that these samples present some crystallized volume fraction even for short periods of heat treatment and are in accordance with DSC results. Importantly, the $LiGe_2(PO_4)_3$-prototype structure has numerous peaks in the XRD diffractograms. They can be confused with the other secondary phases in a usual XRD data treatment based on a simple comparison with the crystallographic patterns. Thus, Rietveld refinement was applied for the samples totally crystallized to confirm the NASICON structure formation. The graphical results of the Rietveld refinement are shown in Figure 2c,d for Sc-free and Sc-containing NASICONs, respectively. The calculated curve overlaps perfectly with the experimental data. No secondary phase was detected. Otherwise, the refinement would diverge. The residual curve is smooth, with specific differences in intensities related to the strongly preferred orientation of the diffraction peaks. This phenomenon is characteristic of XRD data of NASICON compounds,[24,79] which makes their Rietveld refinements challenging.[24] Therefore, the convergence of Rietveld refinement proves that the NASICONs were successfully formed in the heat treatments, and the resulting glass ceramics are primarily composed of this phase. The presence of secondary phases in minor quantities, especially $AlPO_4$, is not discarded, since they have been found by other authors in diverse quantities.[48,72,73] However, the XRD demonstrated that their concentration is below the detection limit of the technique. These results showed the high potentiality of the glass ceramic method to prepare the NASICONs with a high degree of purity. Secondary phases are well known as one of the main problems when NASICONs are prepared by other scalable methods such as solid-state reaction. These phases are usually deposited in the grain boundary region, and most of them block the lithium transport between the grains, reducing the ionic conductivity.[80] The high homogeneity acquired for the melts from the parent glass preparation hinders the cation segregation and favors the polycationic NASICON structure formation. Moreover, the moderate temperature used to melt the precursors also contributed to avoiding lithium volatilization, which would also result in secondary phase formation.

https://doi.org/10.1021/acs.jpcc.3c00476
J. Phys. Chem. C 2023, 127, 6207−6225

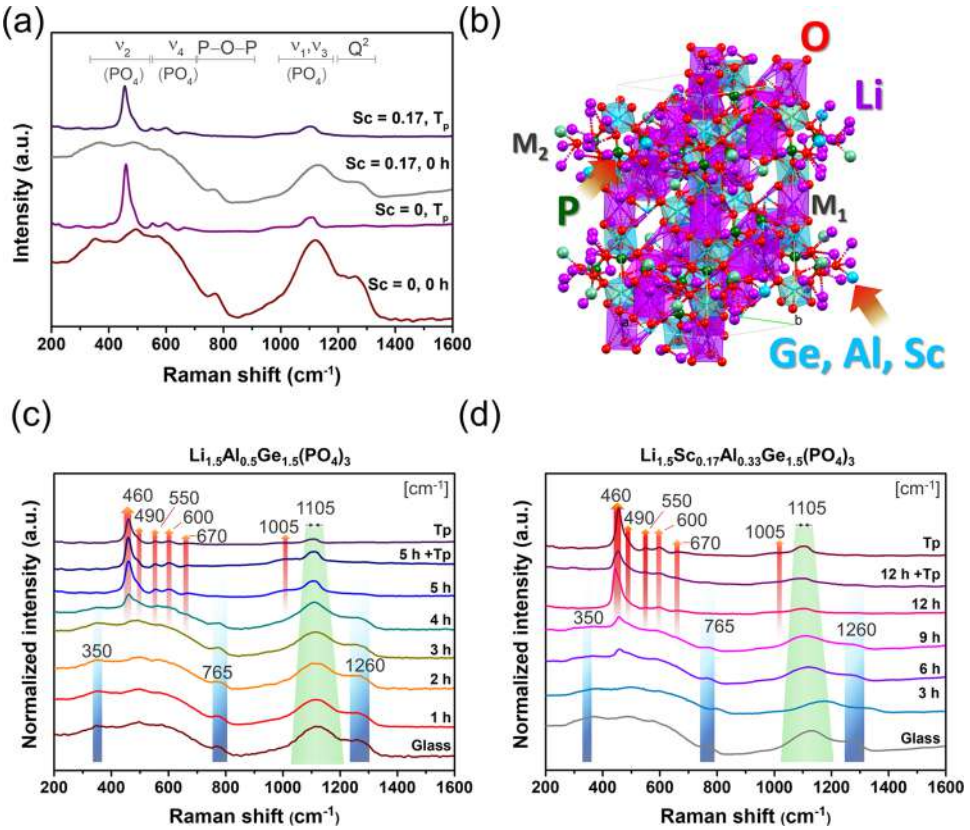

Figure 3. Structural characterization from long- to medium-order spectra of the parent glass and glass ceramics: (a) Comparison of the Raman spectra of the parent glasses and glass ceramics totally crystallized at T_p. The phonon modes are attributed to their probable assignments. (b) Scheme of the rhombohedral structure of a NASICON with typical $Li_{1+x}B^{(III)}_xGe_{2-x}(PO_4)_3$ composition. Examples of M_1 and M_2 interstitial positions are emphasized. (c) Spectral evolution of the samples according to the advance in the heat treatment, along with the patterns heat-treated at T_p (LAGP composition). (d) Spectral evolution of the samples according to the advance in the heat treatment, along with the patterns heat-treated at T_p (LAScGP composition).

The Rietveld method with an internal standard allowed us to perform the estimative of the evolution of the crystallized volume fraction (α) and the evolution of the crystallite sizes (D) of the glass ceramics. Importantly, yttrium oxide was chosen as an internal pattern for these analyses because of the following bullet points. (1) It is an oxide with high purity (99.99% according to the provider). (2) It is monophasic, easing the Rietveld refinement and increasing the precision for phase quantification. (3) It has a cubic structure ($Ia\bar{3}$ space group),[51] reducing the possibility of preferential orientation. (4) The most intense XRD peaks of this material do not overlap with the ones from LAGP and LScAGP. These precautions have been taken to allow the estimation of α by the Internal Standard Method[50] with the highest reliability possible. Once this standard was considered suitable (Figure S1), the X-ray patterns of powdered glass ceramics containing yttrium oxide were refined. The related Rietveld profiles are shown in Figures S2 and S3 for LAGP and LAScGP systems, respectively. Good correspondence of the peaks of the pattern and the NASICON structures was obtained, demonstrating convergence for the refinements. Hence, the results of α and D could be properly estimated. The related results are shown in Table S2. The values of α were also estimated by the reduction of the crystallization peak's area from the DSC measurements. These estimations were made by comparing the exothermic peak of the glass ceramic with that of the fully amorphous glass from the same system. The following relation was used: $\alpha = (1 - (v/V))$, where α is the crystallized volume fraction, v is the crystallization peak area from DSC analysis of the glass ceramic, and V is the same parameter, but for the parent glass absent of any heat treatment. The results are also presented in Table S2. The results of α obtained by these different techniques show the tendency for crystal increment according to the advance of heat treatment. They are concordant with each other, mainly for the LAScGP system and LAGP at the late stages of crystallization. Though, posteriorly in this text, the results of α will be referred to as the ones obtained by Rietveld refinement due to their greater precision for crystallographic assessments. They are also more concordant with the other characterization techniques that will be discussed further. Importantly, for both systems, the D values do not show, at the early stages of crystallization, a clear tendency for growth. This result can be attributed to the strong nucleation phenomenon, that is, a new population of nuclei and crystals is being formed, with no significant growth of the oldest ones. On the other hand, after 3 h for the LAGP system and 9 h for the LAScGP one, a more evident tendency for an increment of the D values is seen. The crystal growing is probably gaining ground for these conditions. We may think on an induction time for crystal growth. Comparing the crystallization advance as a whole, an evident increment of α is seen for the samples. Interestingly, the points in which α becomes dominant in the systems are between 3 and 4 h for the LAGP series, in which α increases from 13 to 86%, and

https://doi.org/10.1021/acs.jpcc.3c00476
J. Phys. Chem. C 2023, 127, 6207−6225

between 9 to 12 h for the LAScGP system, in which α increases from 65 to 98%. As already supposed, the LAScGP system demands more time to be crystallized in the temperature of heat treatment chosen by the same rule (T_g + (T_x − T_g)/3), which is a result of a slower crystallization kinetics. This occurs due to the increment of the glassy phase stability promoted by a higher polarizable cation[69,70] (Sc^{3+}), as already discussed. Interestingly, the presence of scandium also impacted the D values from the samples heat-treated at temperatures lower than T_x. That is, they tended to be smaller. Importantly, crystals much larger than ∼0.2 μm provide low broadening in the diffraction peaks, and the crystal size quantification by this technique decays in precision. The peaks' broadening for these cases is close to the instrumental pattern. So, for samples heat-treated directly at T_p, there is only the information that they have crystals probably coarser than the other samples and they are probably at micrometric scale. In-depth interpretations based on these values are not reliable.

Structurally, the lattice parameters expanded in all directions when Sc^{3+} was inserted into the structure, and consequently the cell volume V: $a = b = 8.2580(1)$ Å, $c = 20.6554(4)$ Å, $V = 1.219.90(4)$ Å^3 for LAGP; and $a = b = 8.2927(1)$ Å, $c = 20.7520(6)$ Å, $V = 1.235.92(5)$ Å^3 for LAScGP. These results came from the XRD data of the samples directly treated at T_p, with the corresponding graphical results of Rietveld refinements shown in Figure 2c,d. The cells' expansion is related to the inclusion of a larger cation in the structure. Specifically, Al^{3+} has a crystal radius of 67.5 pm when it is sited at octahedral coordination, while Sc^{3+} is larger, 88.5 pm in the same chemical environment.[81] Therefore, the partial substitution is expected to expand the lattice parameters, and consequently the cell volume. First, these results validate that Sc^{3+} was successfully introduced into the rhombohedral structure. Moreover, the expansion of the cell in LAGP-based systems is referred to as a good strategy to open the bottlenecks to lithium-ion migration, improving the electrical responses.[16]

To better understand the structural evolution according to the crystallization advance from medium- to long-order point of view, Raman spectroscopy was utilized. The results are shown in Figure 3. Comparing the extremes, namely, parent glasses and glass ceramics with heat treatment at T_p, the spectra considerably change (see Figure 3a). The spectra of the glass and NASICON crystals are in agreement with the ones from the literature.[40] The bands of the glasses are broader, which is a reflex of the medium- to long-range disorder. Formally, the spectra of the parent glasses and the glass ceramics containing NASICON crystals are mainly composed of characteristic phonon modes from phosphate-type units.[24,82] To better understand the discussions of structure evolution at this level, a structural representation for the studied NASICON structure was constructed based on the crystallographic information from Weiss et al.[18] and Macrae et al.[52] (Figure 3b). The NASICON structure with $LiGe_2(PO_4)_3$ prototype is rhombohedral with $R\bar{3}c$ space group. The structure is primarily composed of PO_4 tetrahedra sharing their vertices with BO_6 octahedra (B = Ge^{4+}, mainly, and the substituents Al^{3+} and Sc^{3+}). Lithium ions occupied two distinct interstitial positions in the structure, called M_1 and M_2. The extra-lithium cations that are allowed in the structure through trivalent substitution occupy the M_2 positions. The lithium-ion movement through these interstices provides the effective three-dimensional (3D) conductivity observed for the NASICON electrolytes. The Raman spectroscopy can, therefore, provide the information on how the chemical environment around the phosphate units is being changed according to the crystallization advances.

The evolution of the Raman spectra according to the crystallization advance is presented in Figure 3c,d for Sc-free and Sc-containing samples, respectively. Some bands appeared for the crystals or become sharper and more intense (marked with red-upward arrows in these spectra), while other bands disappeared with the heat treatment (marked with blue bars). Moreover, there were bands that reduced their intensity, but the main difference from the glass to the crystals was the shortening according to the crystallization advance (marked with green bars). The position around the appearance of each phonon mode depends on the phosphate's polymerization degree, Q^n. Phonon modes between 300 and 500 cm^{-1} (at around 350, 460, and 490 cm^{-1}) are attributed to the ν_2 components from symmetrical bending of PO_4 groups ($2A_{1g}$ + $2E_g$).[24,83] The modes at around 460 and 490 cm^{-1} became sharper according to the advance of crystallization. These bands are characteristics of the $LiGe_2(PO_4)_3$-based crystals. On the other hand, phonon modes between 500 and 700 cm^{-1} (at around 550, 600, and 670 cm^{-1}) are attributed to ν_4 components of nonsymmetrical bending of these structural units (A_{1g} + $3E_g$).[40,82] They are present in both glasses and crystals. However, the glass phase comprises distorted and oxygen vacant PO_4 polyhedra. These modes appear in the spectra of the glasses as broad bands and overlapped with each other. This is a clear influence on the medium- to long-range disorder of the amorphous phase. On the other hand, the crystal is more symmetric and these vibrations in the crystals occur closer to the same wavenumber due to the gain of structural symmetry. Hence, these bands are sharper and well resolved in the spectra of the glass ceramics with a large content of crystals.

Between 700 and 900 cm^{-1}, there are modes from meta- and piro-phosphates.[82,84,85] A band is seen in this region (∼765 cm^{-1}), which is only present for the glasses and glass ceramics in the early stages of crystallization. Unsurprisingly, this band disappears for the crystals. Particularly, this phonon mode is attributed to the symmetrical stretching of phosphate tetrahedra with bridging oxygen from Q^1.[83,86,87] The PO_4 tetrahedra do not share their vertices in the NASICON crystals, and also there is no Q^1-type unit for the phosphate (all of them are perfectly tetrahedrally coordinated). Thus, this mode is not expected to appear after crystallization. The extinction of the mode at around 765 cm^{-1} is clear evidence of the consumption of the phosphate-based glassy phase according to the heat treatment.

Phonon modes between 900 cm^{-1} and 1300 cm^{-1} are attributed to stretching modes from PO_4 ($P^{(4)}$) units (ν_1 and ν_3, showing A_{1g} + E_g and A_{1g} + $3E_g$ vibrations), making it hard to distinguish between them.[24,82,83] These modes appear between 1000 and 1110 cm^{-1} for crystals and glasses. The sharpening of these Raman bands and the gain in intensity observed for samples containing crystals occurred gradually with the heat treatment. Once again, the increase of intensity and sharpening of the phonon modes is indicative of the gain of symmetry for the atomic vibrations. Lastly, the broad band at around 1250 cm^{-1} is referred to the $PO_{3(sym)}$ stretching in $P^{(3)}$ units. This band is related to the polyhedra containing nonbridging oxygen.[87,88] This band is also characteristic of the glassy phase and must be extinct for the crystal.[47] That is, all of

https://doi.org/10.1021/acs.jpcc.3c00476
J. Phys. Chem. C 2023, 127, 6207−6225

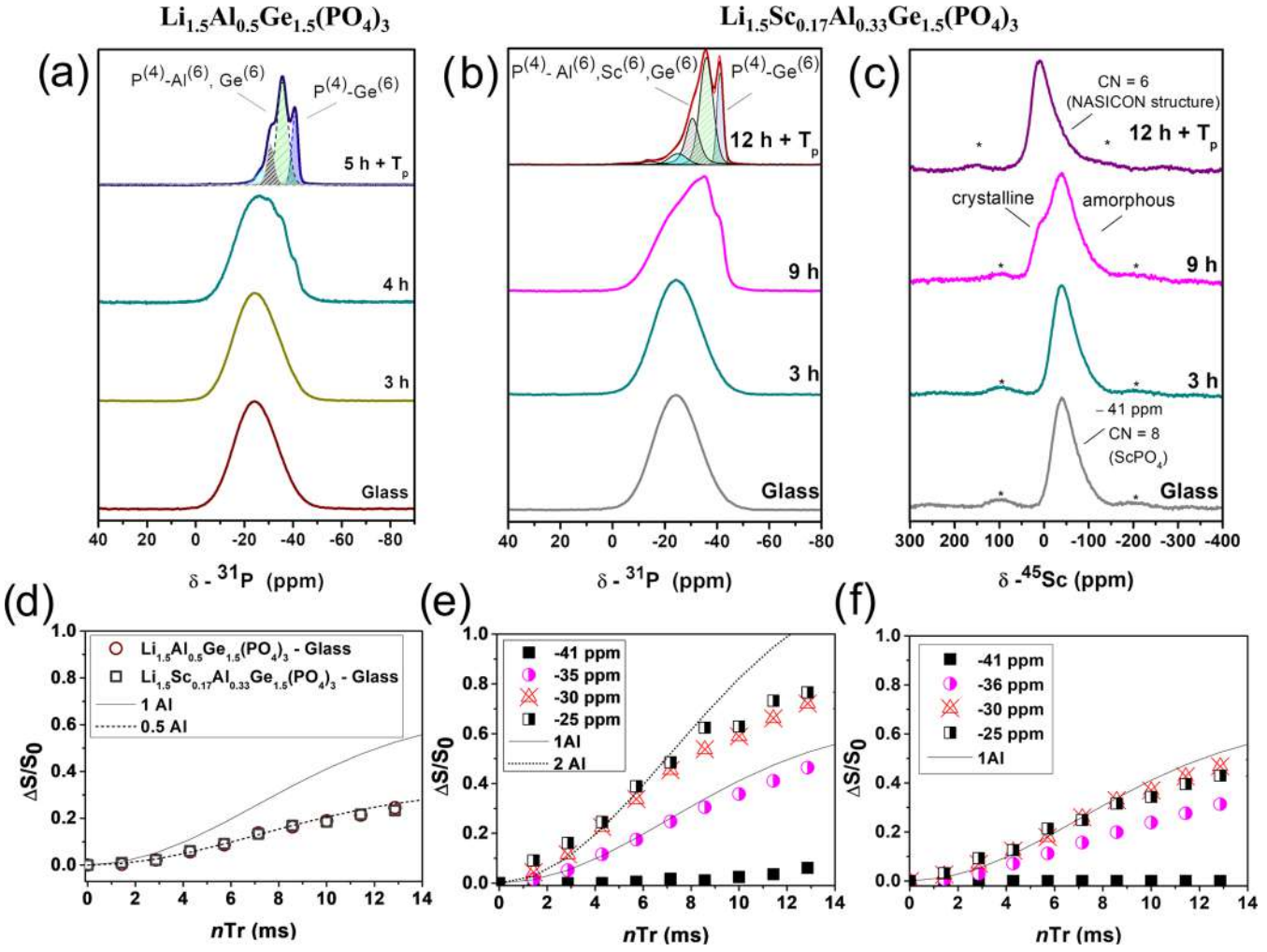

Figure 4. Solid-state NMR spectra and $^{31}P\{^{27}Al\}$ REAPDOR curves for the parent glasses and glass ceramics: (a) ^{31}P spectra for the LAGP series. (b) ^{31}P spectra for the LAScGP series. (c) ^{45}Sc spectra for the $Li_{1.5}Sc_{0.17}Al_{0.33}Ge_{1.5}(PO_4)_3$ series. (d) $^{31}P\{^{27}Al\}$ REAPDOR curves for the glasses with a different composition. (e) $^{31}P\{^{27}Al\}$ REAPDOR curves for the glasses for the fully crystallized sample in the LAGP system (5 h + T_p/1 h). $^{31}P\{^{27}Al\}$ REAPDOR curves for the glasses for a fully crystallized sample in the LAScGP system (12 h + T_p/1 h). Curves from item d to f designate behavior for P−O−Al linkages.

the phosphorous coordination polyhedra are complete in the NASICON crystals, except for ionic defects at an extremely small concentration. The disappearance of this phonon mode demonstrates that the glassy phase is extinct in the glass ceramics, similar to the disappearance of the phonon mode at around 765 cm^{-1}.

The gradual gain of symmetry during the crystallization is evident when analyzed from medium to long range by Raman spectroscopy, corroborating with the XRD results that evidenced the increment of crystallized volume fraction. At a local order, the increment of crystalline nature of the samples is also evident when monitored by solid-state NMR using the ^{31}P, ^{27}Al, and ^{45}Sc nuclei as structural probes. The related results are shown in Figures 4 and 5. The ^{31}P NMR spectra (Figure 4a,b) demonstrate a broad gaussian band centered near −24 ppm for the glass and glass ceramics with short periods of heat treatment. Similar results are seen for both compositions under evaluation. This band is characteristic of phosphate species in different chemical environments, reflecting the isotropic chemical shift distribution from Ge, Al, Sc, and P connections.[89] Importantly, phosphorus is mainly in $P^{(3)}$ units in the glasses. These results are in agreement with REAPDOR evolution experimental data with a SIMPSON two-spin simulation based on a dipolar internuclear $^{31}P-^{27}Al$ distance of 3.3 nm (see Figure 4d),[90] where only a fraction of the P atoms is bonded to Al atoms. The line narrowing is observed for samples submitted to heat treatment up to 4 and 9 h for LAGP and LAScGP systems, respectively, which reflect on δ_{-P} value due to crystalline fraction increasing in the samples. However, the resolution is insufficient to try any deconvolution analysis. For the fully crystallized samples, the ^{31}P local environments shift toward low chemical shift values and the spectra are sharper. They split into up to four partially resolved peaks centered at around −41, −35, −30, and −25 ppm. This result demonstrates that there is a significant difference in the local phosphate environments, confirming the results obtained by Raman spectroscopy. The $P^{(3)}$ units are completely converted into tetrahedrally coordinated phosphorus after crystallization [$P^{(4)}$−($Ge^{(6)}$, $Sc^{(6)}$, $Al^{(6)}$)]. Particularly, the band at around −41 ppm observed for both compositions is related to $P^{(4)}$ surrounded by four Ge octahedrally coordinated and can be assigned to $P_{4Ge}^{(4)}$. These results agree with the structural scheme previously presented in Figure 3b, in which phosphorus tetrahedrally coordinated shares their

https://doi.org/10.1021/acs.jpcc.3c00476
J. Phys. Chem. C 2023, 127, 6207−6225

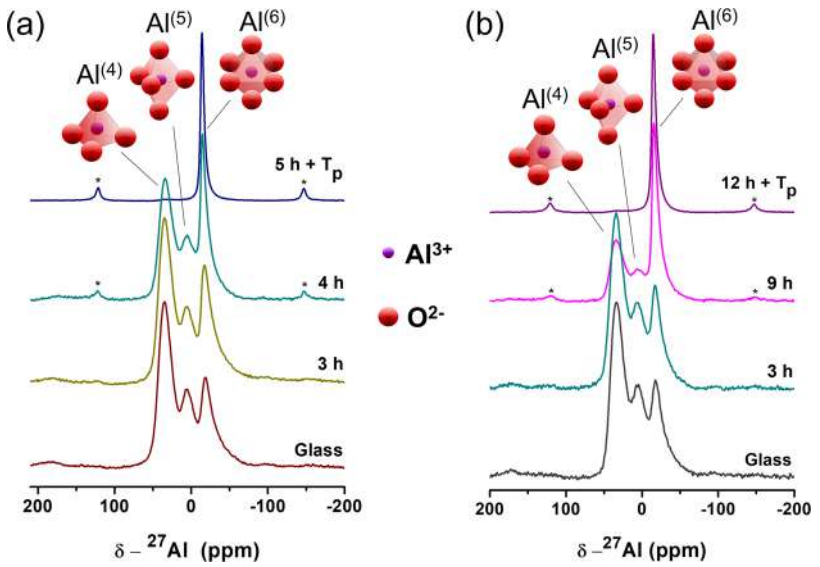

Figure 5. ^{27}Al solid-state NMR spectra for the parent glass and glass ceramics according to the period of heat treatment for different compositions: (a) LAGP series. (b) LAScGP series. Schemes are approximated representations of the coordination polyhedra for aluminum in the glass and glass ceramics. Some distortions in these coordination polyhedra are predictable due to both the long-range disorder of the amorphous phase and also due to the rhombohedral symmetry of the crystals' structure.

polyhedral vertices with germanium octahedrally coordinated in the crystals. The peak at −35 ppm is related to the presence of aluminum in the structure ($P_{3Ge,1Al}^{4}$). This peak at lower chemical shift values is also related to $P^{(4)}$ units but contains both $Al^{(6)}$ and $Ge^{(6)}$ as the next neighbors.[47] These results confirm the site-specific substitution of germanium by aluminum at the octahedrally coordinated sites in the LAGP composition. However, for the LAScGP series, substitutions of Ge^{4+} by Sc^{3+} and Al^{3+} atoms occur simultaneously. The peak multiplicity can arise, therefore, from the formation of such as $P_{(4\text{-}n\text{-}m)Ge,nAl,mSc}^{(4)}$ sites, which can be attributed to ($P_{3Ge,1(Al,Sc)}^{(4)}$) units containing Al^{3+} or Sc^{3+} ions. The formed ($P_{(4\text{-}(m)Ge,mSc)}^{(4)}$) units in the NASICON structure were already observed,[61] and they prove the germanium-to-scandium substitution at octahedrally coordinated sites, along with aluminum. Here in the composition under study, the ^{31}P-{^{27}Al} REAPDOR data confirm the formation of both units ($P_{3Ge,1(Al,Sc)}^{4}$) for the peak contribution at −35 ppm (see Figure 4e,f), where the simulated SIMPSON curve for two-spin interactions is not adjusted for the P atom in this chemical environment. The same behavior was also observed for the peaks at −30 and −25 ppm, indicating the $P_{2Ge,2(Al)}^{(4)}$ units formation, and also the Ge^{4+} is replaced by only an Al^{3+}, forming units such as $P_{(4-1-m)Ge,1Al,mSc}^{(4)}$. Therefore, these results confirm the success of preparing NASICONs structurally modified by dual-cation substitution of germanium at its octahedrally coordinated sites. Importantly, the same evolution behavior is observed for ^{45}Sc MAS NMR results shown in Figure 4c. Table S3 (in the Supporting Information) summarizes the simulated parameters using the Czjzek models for ^{45}Sc MAS NMR, which is based on a distribution of chemical shifts and quadrupolar coupling constants (C_Q).[91] We observed a broad asymmetric peak at −12 ppm for the glass, with a large average quadrupole coupling constant 10.22 MHz, as typically observed for Sc-containing glasses. The Sc^{3+} coordination number is difficult to be estimated because the scandium in six coordinated compounds shows a negative isotropic chemical shift value. All eight coordinated Sc^{3+} cations show a negative isotropic chemical shift; however, in phosphate glasses, the scandium coordination is expected to be six, and the chemical shift range 10−50 ppm. For samples with long heat treatment (9 h) and also for those fully crystallized (12 h + T_p), a new peak appears at 36 ppm. This peak is asymmetric, and it is the only nonspectral signal remaining for the fully crystallized sample, which is attributed to the six-coordinate Sc atom in the NASICON structure.[92]

The ^{27}Al spectra also demonstrate the great change in the material structure comparing the glasses with the glass ceramics. They are in complete accordance with ^{31}P data discussed above. The results are shown in Figure 5. ^{27}Al spectra demonstrate that Al^{3+} can be coordinated by different polyhedra in glasses: $Al^{(4)}$, $Al^{(5)}$, and $Al^{(6)}$.[93,94] Approximate illustrations of these structural units are also presented in Figure 5. This result corroborates with the amorphous nature of these materials, allowing different coordination polyhedra for this cation. Importantly, aluminum tetrahedrally coordinated, $Al^{(4)}$, is the dominant structural unit for Al^{3+} in the glasses for both compositions used. Once the crystallization advanced, the signals from $Al^{(6)}$ become progressively dominant in the system. Aluminum with the other coordination numbers ($Al^{(4)}$ and $Al^{(5)}$) disappears for the totally crystallized sample. The same is observed for ^{27}Al{^{31}P} REDOR experiments performed for both compositions. The related curves are shown in Figure S4, and the fitted parameters are summarized in Table S4, both in the Supporting Information. The results demonstrated that aluminum cations with low coordination numbers are predominant in the glasses, which are completely converted into $Al^{(6)}$ in the crystals. This result confirms once again the propensity for Al^{3+} to be octahedrally coordinated in the NASICON crystals, substituting Ge^{4+}, which presents the same coordination in this chemical environment. Moreover, the absence of other detectable coordination number for aluminum for the fully crystallized glass ceramics is another indication that secondary phases do not remain in expressive quantity. Aluminum can be tetrahedrally coordinated (or even

https://doi.org/10.1021/acs.jpcc.3c00476
J. Phys. Chem. C 2023, 127, 6207−6225

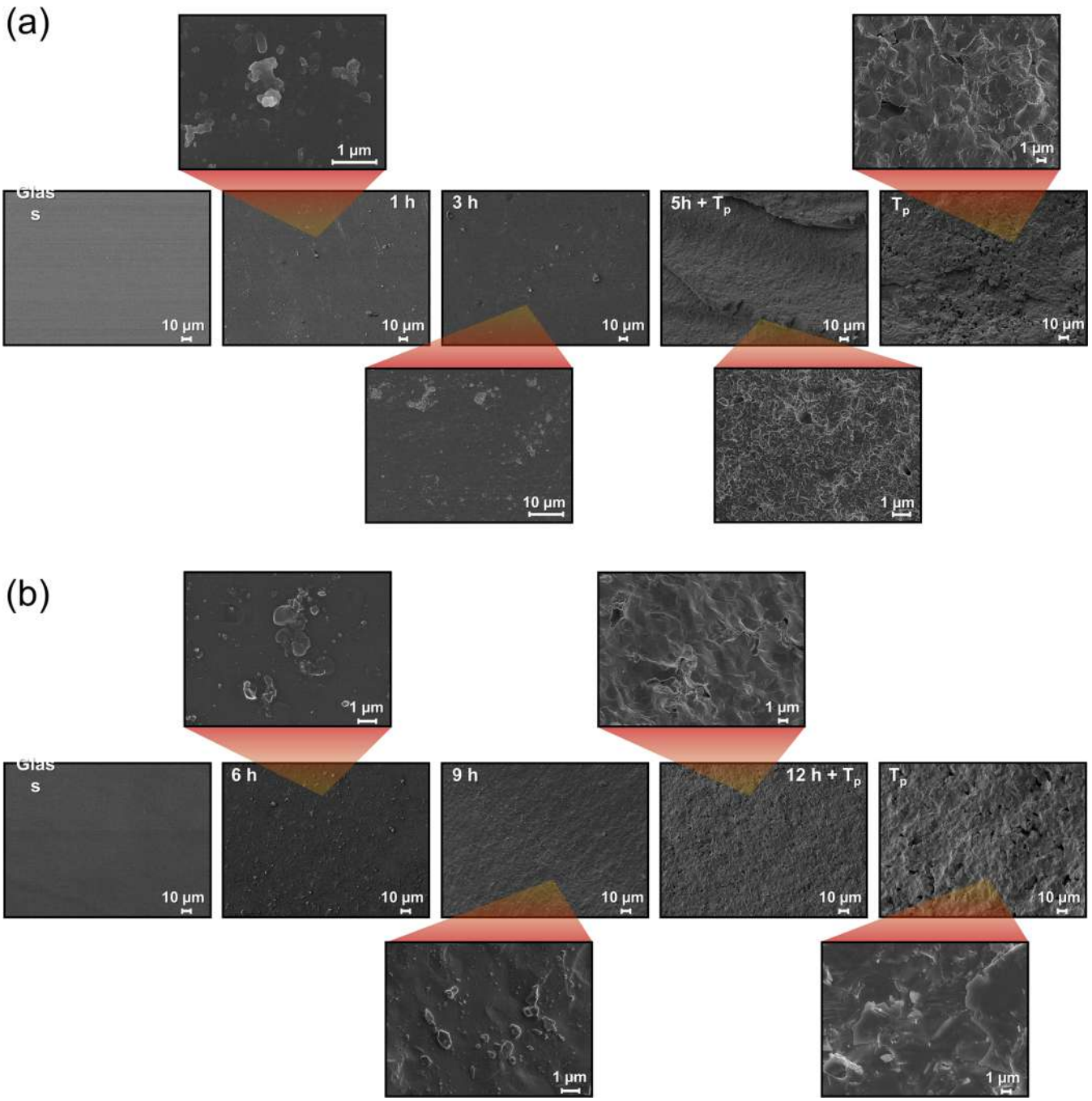

Figure 6. SEM micrographs for the glass ceramics (cracked surfaces) according to the advance of heat treatment: (a) LAGP series and (b) LAScGP series.

fivefold coordinated) even in crystals with other structures due to its small size.[95] An example is $AlPO_4$ that presents Al^{3+} in $Al^{(4)}$ unities and would appear separately in the ^{27}Al MAS NMR spectra.[48] This result corroborates that the crystallization was well processed and a strict compositional control was achieved for the prepared glass ceramics, avoiding secondary phase generation at a detectable level.

3.3. Microstructural and Compositional Characterization. After the structural evolution was investigated from local to long order with details, the microstructure evolution of the glass ceramics is now examined. SEM analysis was applied to directly observe the crystals formed according to the advance of heat treatment. The results are shown in Figure 6. Importantly, the properties of an electrolyte will not depend only on the structure, composition, and crystallographic phases formed in the samples. The way in which these phases are arranged (microstructure) equally impacts the electrical responses. Thus, the advance of crystallization according to the period of heat treatment is evident for both compositions in the SEM images. The glasses have a flat surface, without any evidence of crystals. This is in accordance with the structural characterization discussed before. For short periods of heat treatment (e.g., 1 h for LAGP series, Figure 6a), crystals with low dimensions begin to appear. They are in low quantity and dispersed throughout the whole material, surrounded by the glassy phase. After these small crystals and nuclei are formed,

https://doi.org/10.1021/acs.jpcc.3c00476
J. Phys. Chem. C 2023, 127, 6207−6225

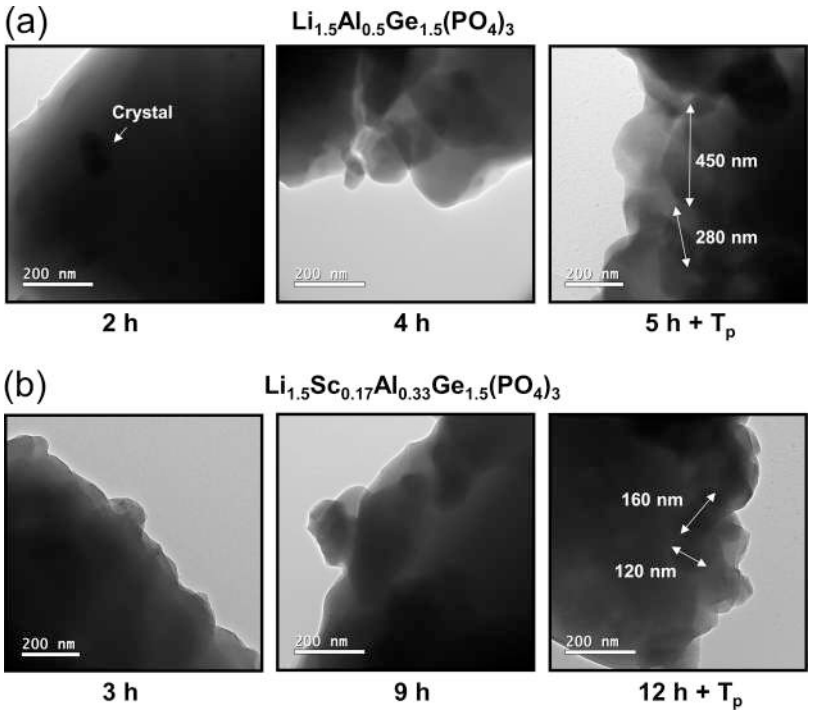

Figure 7. TEM micrographs for the glass ceramics at the beginning, middle, and end of crystallization: (a) LAGP series and (b) LAScGP series.

they contribute themselves to the crystallization advance through the crystal growth on their surfaces. Importantly, the number and size of agglomerate of crystals increase according to the period used for the heat treatment. The samples heat-treated in the maximum period of time followed by 1 h in T_p showed a continuous net of crystals, forming a typical "grain−grain boundary" microstructure. These results support the discussions already made related to the crystallization advance.

The results for both compositions also showed that the grains of the specimens directly treated at T_p are coarser than for samples heat-treated in the maximum period of time and then at T_p. The samples directly treated at T_p received almost "instantly" the energy necessary to totally convert the matrix, composed integrally of glass, into the equilibrium phase (NASICON crystals). Therefore, crystallization happens very quickly, mostly over the athermic nuclei present in low quantity, and large grains are expected to be formed. On the other hand, the samples that were treated at a third of the distance between T_g and T_x showed lower crystallization kinetics. This factor allowed a gradual increase of nuclei quantity, in a number greatly superior to the athermic ones, leading to a larger amount of crystals to be obtained with the heat treatment advance. The crystals, therefore, tend to be smaller. Moreover, only a few portions of the glassy phase remain when these samples are posteriorly heat-treated at T_p. Thus, the microstructure is almost totally defined before the heat treatment at T_p, showing a microstructure composed of small-size crystals. The temperature and time used (T_p for 1 h) are not sufficient to promote an intense growth of these grains already formed, and the resulting microstructures are more refined compared to the ones directly treated on T_p. These observations are important as the microstructure can deeply affect the electrolyte performance.

To complement these analyses, some samples were evaluated by TEM comprising the beginning, middle, and end of crystallization for both systems. The results are shown in Figure 7. The samples begin with small dark spots, presumed to be crystals, dispersed throughout all of the glass matrices. They are more evident in the micrographs for the LAGP system (2 h) and are also present for the LAScGP sample heat-treated for 3 h with lower definition. The presence of crystals dispersed throughout the glass matrix points to a tendency for homogeneous nucleation for the LAGP-based systems as already found in the literature.[45,96] Increasing the time of heat treatment, the crystals become larger. This evidence supports the advance of crystallization already monitored by spectroscopic techniques and also by Rietveld refinements. Though, the dark spots are not completely connected to each other either for LAGP 4 h or LAScGP 9 h, indicating that a considerable amount of glassy phase still remains surrounding the crystals. The presence of a glassy phase around the crystals blocks partially (or even totally) the connection of crystals, and consequently the lithium-ion paths. Finally, for samples heat-treated at the maximum period of heat treatment and followed by T_p, a grouping of crystals can be seen in the images forming the glass ceramics completely crystallized. The "grain−grain boundary" microstructure was indeed formed in these samples, as already demonstrated by SEM. Importantly, the measurements of the sizes of some well-resolved grains in the micrographs of these samples have revealed that the grain sizes for LAScGP glass ceramics (12 h + T_p) are smaller than the ones from LAGP glass ceramics (5 h + T_p). This result is in agreement with the ones from the crystallite sizes, being attributed to slower crystallization kinetics for the samples containing scandium as already discussed. Results such as these are important, once microstructure can have a strong influence on the electrical properties of the glass ceramics.

The SEM and TEM micrographs opened the potentiality to directly evaluate the atomic composition and evaluate possible cationic segregation through EDS mapping. The results of EDS-TEM maps for both compositions are seen in Figure 8.

https://doi.org/10.1021/acs.jpcc.3c00476
J. Phys. Chem. C 2023, 127, 6207−6225

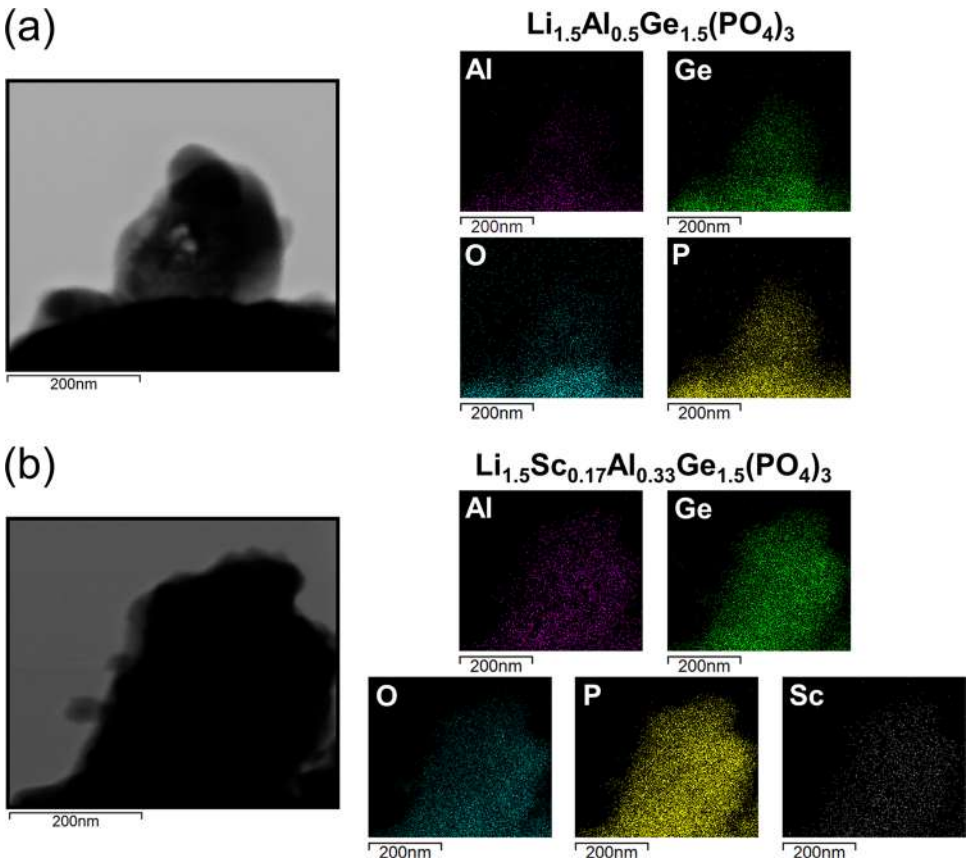

Figure 8. TEM elemental mapping distribution for glass ceramics: (a) LAGP heat-treated for 4 h and (b) LAScGP heat-treated for 9 h.

The samples of LAGP−4 h and LAScGP−9 h were chosen because they have a mix of crystals and glass matrix, allowing the observation of the compositional differences of both (if any). All of the characteristic elements for the NASICON structure appeared in the EDS mapping, except for lithium cations. Lithium was not seen in the chemical maps because it is a light element and is not determined by this technique. The other elements are homogeneously distributed in the glass ceramic of LAGP composition (Figure 8a) and also for LAScGP one (Figure 8b). Interestingly, scandium used as a second substituent other than aluminum could also be determined (Figure 8b). The intensity collected for this element is weak as the mass percentage is lower than 2%. However, its detection and homogeneous dispersion is undoubtful by the TEM-EDS maps shown in Figure 8b. The observation of this element in the mappings confirms the double substitution for this series, corroborating with Rietveld refinement analysis and also the MAS solid-state NMR ones. Importantly, there was not a signal accumulation of any element even at a so small scale of elemental detection. Thus, no evidence of secondary phases could be noticed by this technique. These results are in accordance with the discussions already made. Secondary phases in the glass ceramics prepared are probably at an exceptionally low quantity. Therefore, the process utilized to prepare the glasses and raw materials employed were satisfactory to prepare glass ceramics with great compositional control. To confirm the persistence of these results for the samples totally crystallized, SEM images containing EDS maps for samples LAGP (5 h $+T_p$) and LAScGP (12 h + T_p) are shown in Figure S5. The results are similar to the ones already discussed, demonstrating a homogeneous distribution of the elements through the surface. No evidence for cationic segregation or secondary phase formation was obtained as well. Lastly, the composition of the glassy samples and samples heat-treated for the largest period of time in each system was further evaluated by XRF. The related numerical values for weight percentages are displayed in Table S5. Importantly, the presence of lithium and oxygen was ignored for these analyses and for the references of nominal composition because they are not adequately determined by XFR. The results demonstrated the presence of all of the elements planned for the samples. The content of aluminum decreases for samples prepared with scandium, as expected, while phosphorus and germanium are the main elements that compose these materials. In addition to lithium quantification by ICP-OES, these results corroborate to the presence of the elements expected for the NASICON structure in the systems under evaluation.

3.4. Electrical Properties. Finally, Figure 9 shows the electrical properties of the glass ceramics according to the heat treatment period utilized for their preparation. The analysis of electric properties shows how much the advance of crystallization impacts on the electrical conductivity of the NASICON glass ceramics. The glass ceramics showed distorted semicircles because of the nontotally resolved responses of the crystals and the glass matrix, or even the grain and grain boundaries contribution for the crystallized glass ceramics. Nevertheless, plots like those allow the obtention of the total conductivity of the samples.[97,98] Examples of Nyquist plots for samples from both systems are shown in Figure S6. Importantly, both of the compositions evaluated started with poorly conductive glasses and reach

https://doi.org/10.1021/acs.jpcc.3c00476
J. Phys. Chem. C 2023, 127, 6207−6225

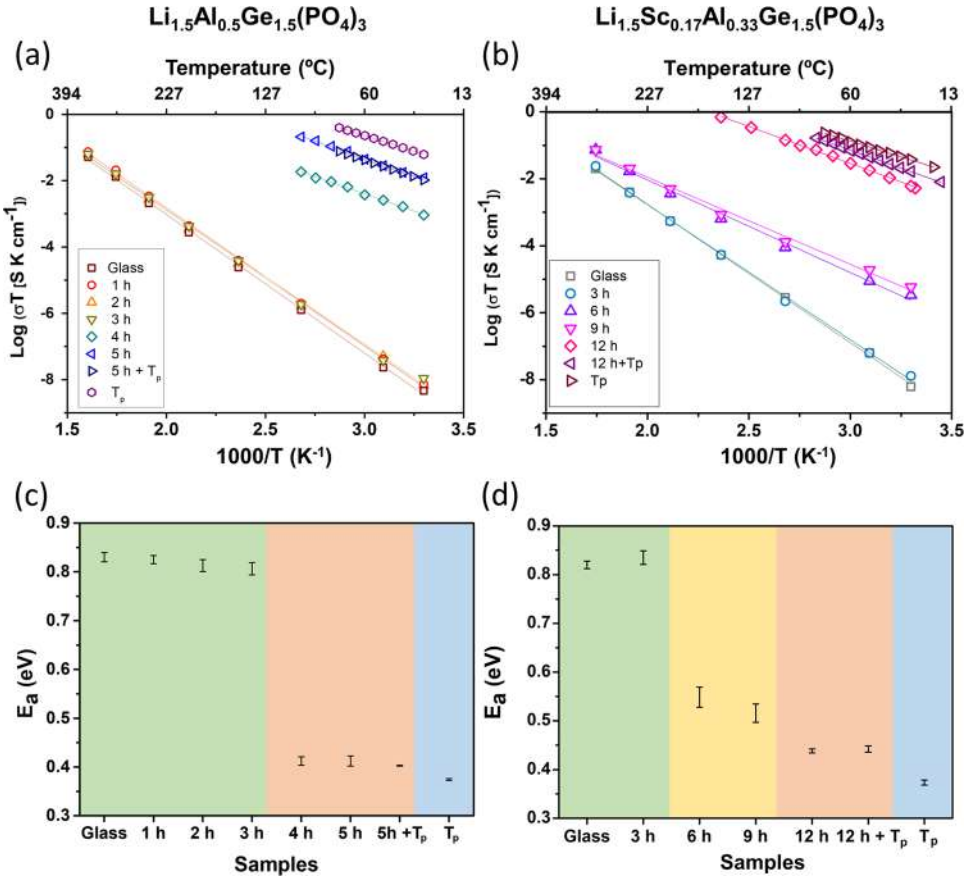

Figure 9. Arrhenius plots of conductivity and activation energy for: (a) LAGP glass ceramics heat-treated for different periods at 542 °C and the samples heat-treated at 542 °C for 5 h followed by T_p (1 h) and directly treated at T_p (1 h). (b) Glass ceramics with LAScGP composition heat-treated for different periods at 577 °C and the samples heat-treated at 577 °C for 12 h followed by T_p (1 h) and directly treated at T_p (1 h). (c) Activation energy for LAGP glass ceramics heat-treated for different periods at 542 °C and the samples heat-treated at 542 °C for 5 h followed by T_p (1 h) and directly treated at T_p (1 h). (d) Activation energy for LAScGP glass ceramics heat-treated for different periods of time at 577 °C and the samples heat-treated at 577 °C for 12 h followed by T_p (1 h) and directly treated at T_p (1 h).

conductive glass ceramics when totally crystallized. However, the increment of conductivity between these extremes does not occur linearly. Observing the Arrhenius plots, samples in the LAGP system (Figure 9a) demonstrated that even containing crystals, glass ceramics prepared up to 3 h present almost the same behavior for conductivity versus temperature as their parent glass. That is, the slope for the Arrhenius linearization is almost the same for samples in this system, which is a reflex of close values of E_a.

Samples in LAScGP series (Figure 9b) showed the same behavior for up to 3 h. That is, crystals formed in the early stages of heat treatment are completely surrounded by the glassy phase and are not in quantity enough to effectively change the electrical properties. After 3 h of heat treatment, the Arrhenius curves are displaced to regions of higher conductivity in the LAGP system, indicating that the conductivity is greatly increased. For the LAScGP series, the change in the Arrhenius plots is seen in two steps: (1) up to 9 h, in which there is a moderate increase of the conductivity and intense change in the curve slope, and (2) a pronounced change of conductivity is seen for samples heat-treated for periods of time greater than 9 h, along with new changes in the slopes of the curves. To better comprehend these modifications, Figure 9c,d shows the behavior for E_a extracted from these plots, with their respective uncertainties arising from the linearization. For the Sc-free system (LAGP), the graph can be, therefore, divided into three regions: (1) The former region up to 3 h of heat treatment, in which the values of E_a for all of the glass ceramics are close to the parent glass (0.83−0.81 eV) and are poorly impacted by the heat treatment. (2) In the second region, the crystals became the mandatory phase. In other words, the grains were put in contact to form a typical "grain−grain boundary" microstructure, i.e., the percolation of crystals has occurred. This fact eases the lithium-ion motion and reduces E_a considerably (0.40−0.41 eV). This phenomenon is in accordance with the XRD results, in which the crystallographic peaks become dominant in the diffractograms after 4 h, while the amorphous halo almost disappeared, and also with the α quantification. Interestingly, the low content of glassy phase that exists for some of these glass ceramics (e.g., LAGP heat-treated for 5 h) poorly impacted E_a. (3) The last region is related to the sample directly treated at T_p, showing that larger grains positively impact the conductivity of these electrolytes. Large grains present lower values of grain boundary area compared to glass ceramics with smaller grains, which eases the lithium-ion motion (E_a = 0.37 eV). For the system containing scandium, the interpretation is similar, but there is an addition of an intermediate region between regions 1 and 2, comprising the samples prepared for 6 and 9 h of heat treatments. This is done because the increment of heat treatment greatly increases the content of crystals (from 10 to 65% in this interval), as it can be seen in the SEM micrographs from Figure 6b. These

https://doi.org/10.1021/acs.jpcc.3c00476
J. Phys. Chem. C 2023, 127, 6207−6225

crystals are in quantity enough to reduce E_a for samples prepared at 6 and 9 h, once the lithium-ion motion promoted by alternating potential is facilitated in the crystals compared to the glass matrix. However, these crystals are still surrounded by the glassy phase. Thus, the content of crystals is high enough to change the activation energy, but are not effectively put in contact with each other to greatly increase the total conductivity. The movement from one crystal to another is still hindered. On the other hand, increasing the heat treatment period to 12 h, the crystal percolation occurred and a "grain−grain boundary" microstructure is formed (α = 98%). This eases the lithium-ion motion between the grains, leading to an effective increment of the conductivity and a new reduction of E_a. The intermediate behavior was seen only for the LAScGP series (6 and 9 h) because of the greater thermal stability of the scandium-containing glass precursor, leading to a lower crystallization kinetic. This allowed an even more gradual increment of crystals compared to Sc-free LAGP. The faster crystallization kinetic of this latter system changed the sample with a low quantity of crystals (3 h, 13 wt %) to a considerably crystallized glass ceramic (4 h, 86 wt %), allowing to reach a more important crystal volume fraction faster and improve both conductivity and E_a. For a more precise analysis, the numerical values of the electrical properties are summarized in Table 1. Note that the conductivity at room temperature only

Table 1. Summary of the Electrical Properties of the NASICON Parent Glasses and Glass Ceramics Prepared by Different Periods of Time

sample	$\sigma_{(30\ °C)}$ (S cm^{-1})	E_a (eV)	R^2
	$Li_{1.5}Al_{0.5}Ge_{1.5}(PO_4)_3$ Series		
glass	1.51×10^{-11}	0.83 ± 0.01	0.999
1 h	2.26×10^{-11}	0.825 ± 0.008	0.999
2 h	2.43×10^{-11}	0.82 ± 0.01	0.998
3 h	3.59×10^{-11}	0.81 ± 0.02	0.998
4 h	3.03×10^{-6}	0.412 ± 0.009	0.997
5 h	4.07×10^{-5}	0.41 ± 0.01	0.996
5 h + T_p	3.50×10^{-5}	0.4027 ± 0.0006	0.999
T_p	2.04×10^{-4}	0.374 ± 0.002	0.999
	$Li_{1.5}Sc_{0.17}Al_{0.33}Ge_{1.5}(PO_4)_3$ Series		
glass	2.03×10^{-11}	0.820 ± 0.008	0.999
3 h	4.27×10^{-11}	0.80 ± 0.01	0.998
6 h	1.12×10^{-8}	0.55 ± 0.02	0.992
9 h	1.94×10^{-8}	0.52 ± 0.02	0.992
12 h	2.01×10^{-5}	0.438 ± 0.004	0.999
12 h + T_p	5.44×10^{-5}	0.442 ± 0.007	0.998
T_p	1.23×10^{-4}	0.373 ± 0.005	0.998

reaches the order of 10^{-4} S cm^{-1} when the crystals become the dominant phase, that is, reaching the crystal percolation. The values of conductivity also confirm that the glass ceramics directly treated at T_p shows higher conductivity due to their large grain sizes. Low content of athermic nuclei during the crystallization at these conditions leads to the formation of a lower number of crystals and coarse microstructures are formed as a consequence, reducing the grain boundary region and increasing the conductivity.

Importantly, in the previous research of our group,[5] we reviewed the methods from the literature for NASICONs preparation, showing principally the influence of the composition, processing, and the related microstructure in the electrical properties of the electrolyte. The results of the present study are comparable to superior to the ones obtained by the solid-state reaction followed by some technique of sintering (usually, E_a > 0.40 eV and $\sigma < 10^{-4}$ S cm^{-1} for LAGP-based systems). This has occurred because of the greater compositional control, denser microstructure, and reduction of secondary phase formation of glass ceramics compared to solid-state reaction synthesis. Comparing the results of the present study with the ones obtained by chemical methods of synthesis, the results are also comparable (in general, E_a in the range of 0.33−0.38 eV and σ in the order of 10^{-4} S cm^{-1} for the LAGP-based systems). Even though showing similar values, the glass ceramics procedure is a scale-up method, easing the practical application of these materials. Lastly, comparing the results of this study with other glass ceramics presenting similar compositions, most of the studies are in the same order of magnitude for the conductivity,[5] but there are examples in the literature of materials with higher conductivity ($\sigma > 10^{-3}$ S cm^{-1}) and lower E_a (as low as 0.28 eV).[16,43,99−101] These observations corroborate that the glass ceramic methodology is a successful strategy to prepare NASICON materials. For these highly conductive glass ceramics from the literature, the microstructure of the glass ceramics totally crystallized was adjusted, mainly, to obtain coarse grains, with low content of pores and secondary phases. Also, the composition was also modified in some of them[16] to open the bottlenecks for lithium migration. Even though the present study presenting lower conductivity and higher activation energy than these latter outstanding studies, the scope here was comprehending the evolution of the electrical properties according to the increment of crystal content and evaluating the changes in structure and microstructure during this process. All of the crystallization conditions were set to achieve these goals.

Yet, our results indicate that even though the presence of scandium directly modifies the crystallization kinetics and leads to a lattice expansion, the final values of electrical properties of the electrolytes totally crystallized are analogous to the ones obtained with the system free of this substituent. This occurs because more refined microstructures are obtained when scandium is present in the glass ceramics, which increases the resistivity of the electrolyte due to a greater grain-boundary area. In previous studies of NASICONs from other systems, a tendency to a decrease in ionic conductivity according to the reduction of the grain sizes was demonstrated.[102] Thus, the improvement of the material's conductivity expected due to the opening of the bottlenecks for the lithium-ion migration is overshadowed by the reduction of the grain sizes, and the final results become comparable. This fact demonstrates once again that the microstructure can impact the final properties of a solid electrolyte as much as the chemical structure. Both of them must be taken into consideration together in order to prepare materials with improved ionic conductivity.

4. CONCLUSIONS

In this paper, an in-depth study of structural and microstructural evolution during the crystallization of $Li_{1.5}Al_{0.5}Ge_{1.5}(PO_4)_3$ and $Li_{1.5}Sc_{0.17}Al_{0.33}Ge_{1.5}(PO_4)_3$ NASICON-type glass ceramics was made, as well as its correlation with their electrical properties. The conclusions of this study can be summarized in the following key points. (1) Parent glasses prepared at moderate melting temperature with proper aluminum source can provide the preparation of glass ceramics free of detectable secondary phases and contamination. (2)

https://doi.org/10.1021/acs.jpcc.3c00476
J. Phys. Chem. C 2023, 127, 6207−6225

Scandium increases the thermal stabilities of the glasses and consequently the time required to achieve fully crystallization. (3) The presence of scandium cation expands the unit cell of the studied NASICON due to its larger size compared to aluminum. (4) Once most of the atomic vibrations in glasses and crystals are different, Raman is a less-explored but potential technique to monitor the crystallization advance in NASICON glass ceramics. (5) Phosphorus is mainly in $P^{(3)}$ unities in the NASICON parent glasses that are completely converted to $P^{(4)}$ unities linked to Ge, Al, and Sc (when applicable) as their next neighbors. (6) The proportion of $Al^{(6)}$ unities compared to four- and fivefold coordinated unities greatly increase in the specimens with the crystallization advance. In fact, $Al^{(4)}$ and $Al^{(5)}$ are completely converted into $Al^{(6)}$ for the NASICON crystals. (7) Scandium is eightfold coordinated in the glasses, but during the crystallization, the preferred site becomes the $Sc^{(6)}$ unities. This result proves that the preferred site of this element is into the octahedral positions in the crystals, being a substitute for germanium similarly to aluminum. (8) The conductivity does not significantly change with the heat treatment up to the formation of a net of crystals, creating a lithium-ion path between the grains. After that, this parameter harshly increases. (9) Larger crystals provide lower activation energy for ion motion and higher conductivity due to a lower grain boundary area compared to a more refined microstructure. This is especially important to be taken into consideration when scandium is used, as it can reduce the crystal sizes of the electrolyte due to a lower crystallization kinetic, which can be detrimental to ionic conductivity.

Therefore, this study brought key points to better understand the crystallization of the NASICON glass ceramics and its correlation with the materials' electrical properties. These insights can be used as tools to tailor the crystallization and the final microstructure of the NASICON glass ceramics, aiming to achieve improved electrical properties.

■ ASSOCIATED CONTENT

Supporting Information

The Supporting Information is available free of charge at https://pubs.acs.org/doi/10.1021/acs.jpcc.3c00476.

Characterization of the internal pattern; results of ICP-OES for lithium determination; graphical results of Rietveld refinements containing Y_2O_3 as an internal standard; results of crystallized volume fraction and crystallite sizes; summary of ^{45}Sc MAS NMR spectral parameters; $^{27}Al\{^{31}P\}$ REDOR results; summary of ^{27}Al MAS NMR spectral deconvolution parameters isotropic chemical shift, area contributions, and values second moments $M_{2(Al\text{-}P)}$ obtained from $^{27}Al\{^{31}P\}$ REDOR experiments; SEM elemental mapping distribution; quantitative results of XRF analyses; and Nyquist plots (PDF)

■ AUTHOR INFORMATION

Corresponding Authors

Jeferson A. Dias − *Chemical and Physical Phenomena Laboratory—LQF, Institute of Science and Technology—ICTIN, Federal University of Lavras (UFLA), São Sebastião do Paraíso, Minas Gerais 37950-000, Brazil; Photonic Materials Laboratory—LMF, Institute of Chemistry, São Paulo State University, Araraquara, São Paulo 14800-900, Brazil;* orcid.org/0000-0001-8066-3784; Email: jefersondias@ufla.br

Silvia H. Santagneli − *Photonic Materials Laboratory—LMF, Institute of Chemistry, São Paulo State University, Araraquara, São Paulo 14800-900, Brazil;* orcid.org/0000-0002-5456-6347; Email: silvia.santagneli@unesp.br

Authors

Ana C. M. Rodrigues − *Vitreous Materials Laboratory—LaMaV, Department of Materials Engineering, Federal University of São Carlos, São Carlos, São Paulo 13565-905, Brazil;* orcid.org/0000-0003-1689-796X

Naiza V. Bôas − *Laboratory of Inorganic and Vitreous Materials—LaMIV, São Carlos Institute of Chemistry, University of São Paulo, São Carlos, São Paulo 13566-590, Brazil;* orcid.org/0000-0002-2190-7707

Younès Messaddeq − *Centre for Optics, Photonics and Lasers—COPL, Faculty of Science and Engineering, Laval University, Quebec, Quebec G1V 0A, Canada;* orcid.org/0000-0002-0868-2726

Complete contact information is available at: https://pubs.acs.org/10.1021/acs.jpcc.3c00476

Author Contributions

The manuscript was written through contributions of all authors. All authors have given approval to the final version of the manuscript and have contributed equally.

Notes

The authors declare no competing financial interest.

■ ACKNOWLEDGMENTS

The authors thank the Faperg project grant 2019/15227-7, SPEC project grant #2015/22828-6, the NMR funding support #2018/24735-3, and also the postdoctoral fellowship of J.A.D. #2019/25756-7, all of them from São Paulo Research Foundation (FAPESP). They also thank the Institute of Chemistry of UNESP (GFQM's laboratory, specially Neide Perruci for kindly performing the XRD analysis as often as requested), Institute of Chemistry of USP (in particular Dr. Mônica Freitas for the special care in the TEM analysis), and Department of Materials Engineering (LaMaV, particularly M.Sc. Vinicius Zallocco for the help with DSC analysis, CCDM, and LCE-UFSCar) for the general facilities. Finally, the authors thank Jane G. Coury (from Publications, Brazil) for carefully revising this paper.

■ ABBREVIATIONS

NASICON, Na^+ super ionic conductor; σ, ionic conductivity; E_a, activation energy for ionic conduction; LAGP, $Li_{1.5}Al_{0.5}Ge_{1.5}(PO_4)_3$; LAScGP, $Li_{1.5}Sc_{0.17}Al_{0.33}Ge_{1.5}(PO_4)_3$; DSC, differential scanning calorimetry; XRD, X-ray diffractometry; MAS NMR, magic angle spinning solid-state nuclear magnetic resonance spectroscopy; FEG SEM, field emission gun scanning electron microscopy; EDS, energy-dispersive X-ray spectroscopy; TEM, transmission electron microscopy; ICP-OES, inductively coupled plasma-optical emission spectroscopy; REDOR, $^{27}Al\{^{31}P\}$ rotational echo double resonance; REAPDOR, $^{31}P\{^{27}Al\}$ rotational echo adiabatic passage double resonance; NT_r, dipolar evolution time; S_0, signal amplitudes without ^{31}P pulsed irradiation; S, signal amplitudes with ^{31}P pulsed irradiation; ΔS, difference signals; T, temperature; k_B, Boltzmann constant; σ_0, preexponential

https://doi.org/10.1021/acs.jpcc.3c00476
J. Phys. Chem. C 2023, 127, 6207−6225

factor; T_g, glass-transition temperature; T_x, onset of crystallization; T_p, crystallization peak; α, crystallized volume fraction; v, crystallization peak area from DSC analysis of the glass ceramic; V, crystallization peak area from DSC analysis of the parent glass; D, crystallite size

REFERENCES

(1) Chen, M.; Hua, W.; Xiao, J.; Cortie, D.; Chen, W.; Wang, E.; Hu, Z.; Gu, Q.; Wang, X.; Indris, S.; et al. NASICON-Type Air-Stable and All-Climate Cathode for Sodium-Ion Batteries with Low Cost and High-Power Density. *Nat. Commun.* **2019**, *10*, No. 1480.

(2) Chen, M.; Hua, W.; Xiao, J.; Zhang, J.; Lau, V. W. H.; Park, M.; Lee, G. H.; Lee, S.; Wang, W.; Peng, J.; et al. Activating a Multielectron Reaction of NASICON-Structured Cathodes toward High Energy Density for Sodium-Ion Batteries. *J. Am. Chem. Soc.* **2021**, *143*, 18091−18102.

(3) Jaumaux, P.; Wu, J.; Shanmukaraj, D.; Wang, Y.; Zhou, D.; Sun, B.; Kang, F.; Li, B.; Armand, M.; Wang, G. Non-Flammable Liquid and Quasi-Solid Electrolytes toward Highly-Safe Alkali Metal-Based Batteries. *Adv. Funct. Mater.* **2021**, *31*, No. 2008644.

(4) Goodenough, J. B.; Hong, H. Y. P.; Kafalas, J. A. Fast Na^+-Ion Transport in Skeleton Structures. *Mater. Res. Bull.* **1976**, *11*, 203−220.

(5) Dias, J. A.; Santagneli, S. H.; Messaddeq, Y. Methods for Lithium Ion NASICON Preparation: From Solid-State Synthesis to Highly Conductive Glass-Ceramics. *J. Phys. Chem. C* **2020**, *124*, 26518−26539.

(6) Venkateswara Rao, A.; Veeraiah, V.; Prasada Rao, A. V.; Kishore Babu, B. Effect of Fe^{3+} Doping on the Structure and Conductivity of $LiTi_2(PO_4)_3$. *Res. Chem. Intermed.* **2015**, *41*, 2307−2315.

(7) Liu, Y.; Chen, J.; Gao, J. Preparation and Chemical Compatibility of Lithium Aluminum Germanium Phosphate Solid Electrolyte. *Solid State Ionics* **2018**, *318*, 27−34.

(8) Lancel, G.; Stevens, P.; Toussaint, G.; Maréchal, M.; Krins, N.; Bregiroux, D.; Laberty-Robert, C. Hybrid Li Ion Conducting Membrane as Protection for the Li Anode in an Aqueous Li-Air Battery: Coupling Sol-Gel Chemistry and Electrospinning. *Langmuir* **2017**, *33*, 9288−9297.

(9) Zhao, W.; Guo, L.; Ding, M.; Huang, Y.; Yang, H. Y. Ultrahigh-Desalination-Capacity Dual-Ion Electrochemical Deionization Device Based on $Na_3V_2(PO_4)_3$@C-AgCl Electrodes. *ACS Appl. Mater. Interfaces* **2018**, *10*, 40540−40548.

(10) Zhang, X.; Rui, X.; Chen, D.; Tan, H.; Yang, D.; Huang, S.; Yu, Y. $Na_3V_2(PO_4)_3$: An Advanced Cathode for Sodium-Ion Batteries. *Nanoscale* **2019**, *11*, 2556−2576.

(11) Li, S.; Xu, X.; Yao, Z.; Jiang, X.; Huan, Y.; Hu, X.; Chen, W.; Wei, T. A Comparative Study on the Li^+/Na^+ Transportation in NASICON-Type Electrolytes. *J. Phys. Chem. C* **2018**, *122*, 20565−20570.

(12) Tamura, S.; Highchi, T.; Imanaka, N. High Ag^+ Ion Conduction in NASICON-Type Solids. *Electrochem. Solid-State Lett.* **2010**, *13*, F13.

(13) Gandi, S. S.; Gandi, S.; Katari, N. K.; Dutta, D. P.; Ravuri, B. R. Electrical Properties and Scaling Studies of $Na_{3+x}Zr_xSc_{2-x}(PO_4)_3$ Glass Ceramic Electrolyte for Use in Na-Ion Batteries. *Appl. Phys. A: Mater. Sci. Process.* **2019**, *125*, No. 92.

(14) Inaguma, Y.; Funayama, K.; Aimi, A.; Mori, D.; Hamasaki, Y.; Ueda, K.; Ikeda, M.; Ohno, T.; Mitsuishi, K. Effect of Lithium Isotopes on the Phase Transition in NASICON-Type Lithium-Ion Conductor $LiZr_2(PO_4)_3$. *Solid State Ionics* **2018**, *321*, 29−33.

(15) He, S.; Xu, Y.; Zhang, B.; Sun, X.; Chen, Y.; Jin, Y. Unique Rhombus-like Precursor for Synthesis of $Li_{1.3}Al_{0.3}Ti_{1.7}(PO_4)_3$ Solid Electrolyte with High Ionic Conductivity. *Chem. Eng. J.* **2018**, *345*, 483−491.

(16) Nikodimos, Y.; Tsai, M.-C.; Abrha, L. H.; Weldeyohannis, H. H.; Chiu, S.-F.; Bezabh, H. K.; Shitaw, K. N.; Fenta, F. W.; Wu, S.-H.; Su, W.-N.; et al. Al-Sc Dual Doped $LiGe_2(PO_4)_3$ - a NASICON-Type Solid Electrolyte with Improved Ionic Conductivity. *J. Mater. Chem. A* **2020**, *8*, 11302−1313.

(17) Maldonado-Manso, P.; Losilla, E. R.; Martínez-Lara, M.; Aranda, M. A. G.; Bruque, S.; Mouahid, F. E.; Zahir, M. High Lithium Ionic Conductivity in the $Li_{1+x}Al_xGe_yTi_{2-x-y}(PO_4)_3$ NASICON Series. *Chem. Mater.* **2003**, *15*, 1879−1885.

(18) Weiss, M.; Weber, D. A.; Senyshyn, A.; Janek, J.; Zeier, W. G. Correlating Transport and Structural Properties in $Li_{1+x}Al_xGe_{2-x}(PO_4)_3$ (LAGP) Prepared from Aqueous Solution. *ACS Appl. Mater. Interfaces* **2018**, *10*, 10935−10944.

(19) Novikova, S. A.; Il'in, A. B.; Zhilyaeva, N. A.; Yaroslavtsev, A. B. Catalytic Activity of $Li_{1+x}Hf_{2-x}In_x(PO_4)_3$-Based NASICON-Type Materials for Ethanol Conversion Reactions. *Inorg. Mater.* **2018**, *54*, 676−682.

(20) Small, L. J.; Wheeler, J. S.; Ihlefeld, J. F.; Clem, P. G.; Spoerke, E. D. Enhanced Alkaline Stability in a Hafnium-Substituted NaSICON Ion Conductor. *J. Mater. Chem. A* **2018**, *6*, 9691−9698.

(21) Yao, P.; Yu, H.; Ding, Z.; Liu, Y.; Lu, J.; Lavorgna, M.; Wu, J.; Liu, X. Review on Polymer-Based Composite Electrolytes for Lithium Batteries. *Front. Chem.* **2019**, *7*, No. 522.

(22) Zhao, N.; Khokhar, W.; Bi, Z.; Shi, C.; Guo, X.; Fan, L. Z.; Nan, C. W. Solid Garnet Batteries. *Joule* **2019**, *3*, 1190−1199.

(23) Xiao, Y.; Jun, K.; Wang, Y.; Miara, L. J.; Tu, Q.; Ceder, G.; Xiao, Y.; Jun, K.; Ceder, G. Lithium Oxide Superionic Conductors Inspired by Garnet and NASICON Structures. *Adv. Energy Mater.* **2021**, *11*, No. 2101437.

(24) Francisco, B. E.; Stoldt, C. R.; M'Peko, J. C. Lithium-Ion Trapping from Local Structural Distortions in Sodium Super Ionic Conductor (NASICON) Electrolytes. *Chem. Mater.* **2014**, *26*, 4741−4749.

(25) Rossbach, A.; Tietz, F.; Grieshammer, S. Structural and Transport Properties of Lithium-Conducting NASICON Materials. *J. Power Sources* **2018**, *391*, 1−9.

(26) Pérez-Estébanez, M.; Isasi-Marín, J.; Többens, D. M.; Rivera-Calzada, A.; León, C. A Systematic Study of Nasicon-Type $Li_{1+x}M_xTi_{2-x}(PO_4)_3$ (M: Cr, Al, Fe) by Neutron Diffraction and Impedance Spectroscopy. *Solid State Ionics* **2014**, *266*, 1−8.

(27) Arbi, K.; Lazarraga, M. G.; Chehimi, D. B. H.; Ayadi-Trabelsi, M.; Rojo, J. M.; Sanz, J. Lithium Mobility in $Li_{1.2}Ti_{1.8}R_{0.2}(PO_4)_3$ Compounds (R = Al, Ga, Sc, In) as Followed by NMR and Impedance Spectroscopy. *Chem. Mater.* **2004**, *16*, 255−262.

(28) DeWees, R.; Wang, H. Synthesis and Properties of NaSICON-Type LATP and LAGP Solid Electrolytes. *ChemSusChem* **2019**, *12*, 3713−3725.

(29) Li, S.-c.; Cai, J.-y.; Lin, Z.-x. Phase Relationships and Electrical Conductivity of $Li_{1+x}Ge_{2-x}Al_xP_3O_{12}$ and $Li_{1+x}Ge_{2-x}Cr_xP_3O_{12}$ Systems. *Solid State Ionics* **1988**, *28*−*30*, 1265−1270.

(30) Pershina, S. V.; Antonov, B. D.; Farlenkov, A. S.; Vovkotrub, E. G. Glass-Ceramics in $Li_{1+x}Al_xGe_{2-x}(PO_4)_3$ System: The Effect of Al_2O_3 Addition on Microstructure, Structure and Electrical Properties. *J. Alloys Compd.* **2020**, *835*, No. 155281.

(31) Kahlaoui, R.; Arbi, K.; Jimenez, R.; Sobrados, I.; Sanz, J.; Ternane, R. Influence of Preparation Temperature on Ionic Conductivity of Titanium-Defective $Li_{1+4x}Ti_{2-x}(PO_4)_3$ NASICON-Type Materials. *J. Mater. Sci.* **2020**, *55*, 8464−8476.

(32) Duluard, S.; Paillassa, A.; Puech, L.; Vinatier, P.; Turq, V.; Rozier, P.; Lenormand, P.; Taberna, P. L.; Simon, P.; Ansart, F. Lithium Conducting Solid Electrolyte $Li_{1.3}Al_{0.3}Ti_{1.7}(PO_4)_3$ Obtained via Solution Chemistry. *J. Eur. Ceram. Soc.* **2013**, *33*, 1145−1153.

(33) Zhu, Y.; Wu, T.; Sun, J.; Kotobuki, M. Highly Conductive Lithium Aluminum Germanium Phosphate Solid Electrolyte Prepared by Sol-Gel Method and Hot-Pressing. *Solid State Ionics* **2020**, *350*, No. 115320.

(34) Bhanja, P.; Senthil, C.; Patra, A. K.; Sasidharan, M.; Bhaumik, A. NASICON Type Ordered Mesoporous Lithium-Aluminum-Titanium-Phosphate as Electrode Materials for Lithium-Ion Batteries. *Microporous Mesoporous Mater.* **2017**, *240*, 57−64.

(35) Cretin, M.; Fabry, P. Comparative Study of Lithium Ion Conductors in the System $Li_{1+x}Al_xA_{2-x}^{IV}(PO_4)_3$ with A^{IV} = Ti or Ge and $0 \leq x \leq 0.7$ for Use as Li^+ Sensitive Membranes. *J. Eur. Ceram. Soc.* **1999**, *19*, 2931−2940.

https://doi.org/10.1021/acs.jpcc.3c00476
J. Phys. Chem. C 2023, 127, 6207−6225

(36) Yan, B.; Kang, L.; Kotobuki, M.; Wang, F.; Huang, X.; Song, X.; Jiang, K. NASICON-Structured Solid-State Electrolyte $Li_{1.5}Al_{0.5-x}Ga_xGe_{1.5}(PO_4)_3$ Prepared by Microwave Sintering. *Mater. Technol.* **2018**, *34*, 356−360.
(37) Perez-Estébanez, M.; Peiteado, M.; Caballero, A. C.; Palomares, F. J.; Nygren, M.; Isasi-Marín, J. SPS Driven Lithium Differential Diffusion in NASICON-like Structures. *Bol. Soc. Esp. Ceram. Vidrio* **2016**, *55*, 38−44.
(38) Xu, X.; Wen, Z.; Yang, X.; Chen, L. Dense Nanostructured Solid Electrolyte with High Li-Ion Conductivity by Spark Plasma Sintering Technique. *Mater. Res. Bull.* **2008**, *43*, 2334−2341.
(39) Lee, J. S.; Chang, C. M.; Lee, Y. Il.; Lee, J. H.; Hong, S. H. Spark Plasma Sintering (SPS) of NASICON Ceramics. *J. Am. Ceram. Soc.* **2004**, *87*, 305−307.
(40) Pershina, S. V.; Pankratov, A. A.; Vovkotrub, E. G.; Antonov, B. D. Promising High-Conductivity $Li_{1.5}Al_{0.5}Ge_{1.5}(PO_4)_3$ Solid Electrolytes: The Effect of Crystallization Temperature on the Microstructure and Transport Properties. *Ionics* **2019**, *25*, 4713−4725.
(41) Shao, Y.; Zhong, G.; Lu, Y.; Liu, L.; Zhao, C.; Zhang, Q.; Hu, Y. S.; Yang, Y.; Chen, L. A Novel NASICON-Based Glass-Ceramic Composite Electrolyte with Enhanced Na-Ion Conductivity. *Energy Storage Mater.* **2019**, *23*, 514−521.
(42) Eckert, H.; Martins Rodrigues, A. C. Ion-Conducting Glass-Ceramics for Energy-Storage Applications. *MRS Bull.* **2017**, *42*, 206−212.
(43) He, K.; Xie, P.; Zu, C.; Wang, Y.; Li, B.; Han, B.; Rong, M. Z.; Zhang, M. Q. A Facile and Scalable Process to Synthesize Flexible Lithium Ion Conductive Glass-Ceramic Fibers. *RSC Adv.* **2019**, *9*, 4157−4161.
(44) Kotobuki, M.; Koishi, M. Preparation of $Li_{1.3}Al_{0.3}Ti_{1.7}(PO_4)_3$ Solid Electrolyte via a Sol-Gel Method Using Various Ti Sources. *J. Asian Ceram. Soc.* **2020**, *8*, 891−897.
(45) Cruz, A. M.; Ferreira, E. B.; Rodrigues, A. C. M. Controlled Crystallization and Ionic Conductivity of a Nanostructured $LiAlGePO_4$ Glass-Ceramic. *J. Non-Cryst. Solids* **2009**, *355*, 2295−2301.
(46) Vizgalov, V. A.; Nestler, T.; Vyalikh, A.; Bobrikov, I. A.; Ivankov, O. I.; Petrenko, V.; Avdeev, M. V.; Yashina, L. V.; Itkis, D. M. The Role of Glass Crystallization Processes in Preparation of High Li-Conductive NASICON-Type Ceramics. *CrystEngComm* **2019**, *21*, 3106−3115.
(47) Santagneli, S. H.; Baldacim, H. V. A.; Ribeiro, S. J. L.; Kundu, S.; Rodrigues, A. C. M.; Doerenkamp, C.; Eckert, H. Preparation, Structural Characterization, and Electrical Conductivity of Highly Ion-Conducting Glasses and Glass Ceramics in the System $Li_{1+x}Al_xSn_yGe_{2-(x+y)}(PO_4)_3$. *J. Phys. Chem. C* **2016**, *120*, 14556−14567.
(48) Vizgalov, V. A.; Nestler, T.; Trusov, L. A.; Bobrikov, I. A.; Ivankov, O. I.; Avdeev, M. V.; Motylenko, M.; Brendler, E.; Vyalikh, A.; Meyer, D. C.; Itkis, D. M. Enhancing Lithium-Ion Conductivity in NASICON Glass-Ceramics by Adding Yttria. *CrystEngComm* **2018**, *20*, 1375−1382.
(49) Toby, B. H. EXPGUI, a Graphical User Interface for GSAS. *J. Appl. Crystallogr.* **2001**, *34*, 210−213.
(50) Madsen, I. C.; Scarlett, N. V. Y.; Kern, A. Description and survey of methodologies for the determination of amorphous content via X-ray powder diffraction. *Z. Kristallogr.—Cryst. Mater.* **2011**, *226*, 944−955.
(51) Nagarajan, R.; Kumari, P. Antimony Substitution Leading to Structural Transformation (Bixbyite→ Fluorite) and Altering the Optical Band Gap in Y_2O_3. *J. Alloys Compd.* **2021**, *863*, No. 158733.
(52) Macrae, C. F.; Sovago, I.; Cottrell, S. J.; Galek, P. T. A.; McCabe, P.; Pidcock, E.; Platings, M.; Shields, G. P.; Stevens, J. S.; Towler, M.; Wood, P. A. Mercury 4.0: From Visualization to Analysis, Design and Prediction. *J. Appl. Crystallogr.* **2020**, *53*, 226−235.
(53) Dilawar Sharma, N.; Singh, J.; Vijay, A.; Samanta, K.; Dogra Pandey, S. Investigations of Anharmonic Effects via Phonon Mode Variations in Nanocrystalline Dy_2O_3, Gd_2O_3 and Y_2O_3. *J. Raman Spectrosc.* **2017**, *48*, 822−828.
(54) Abrashev, M. V.; Todorov, N. D.; Geshev, J. Raman Spectra of R_2O_3 (R—Rare Earth) Sesquioxides with C-Type Bixbyite Crystal Structure: A Comparative Study. *J. Appl. Phys.* **2014**, *116*, No. 103508.
(55) Ubaldini, A.; Carnasciali, M. M. Raman Characterisation of Powder of Cubic RE_2O_3 (RE = Nd, Gd, Dy, Tm, and Lu), Sc_2O_3 and Y_2O_3. *J. Alloys Compd.* **2008**, *454*, 374−378.
(56) Wang, C. H.; Shu, W.; Qing, Y.; Luo, F.; Zhu, D.; Zhou, W. Lattice Dynamics of Yttria: A Combined Investigation from Spectrum Measurements and First-Principle Calculations. *J. Am. Ceram. Soc.* **2021**, *104*, 1797−1805.
(57) Repelin, Y.; Proust, C.; Husson, E.; Beny, J. M. Vibrational Spectroscopy of the C-Form of Yttrium Sesquioxide. *J. Solid State Chem.* **1995**, *118*, 163−169.
(58) Larson, A. C.; Dreele, R. B. V. *GSAS: General Structure Analysis System*, Los Alamos National Laboratory Report; Los Alamos National Laboratory, 2004.
(59) Medek, A.; Harwood, J. S.; Frydman, L. Multiple-Quantum Magic-Angle Spinning NMR: A New Method for the Study of Quadrupolar Nuclei in Solids. *J. Am. Chem. Soc.* **1995**, *117*, 12779−12787.
(60) Amoureux, J. P.; Fernandez, C.; Steuernagel, S. ZFiltering in MQMAS NMR. *J. Magn. Reson., Ser. A* **1996**, *123*, 116−118.
(61) d'Anciães Almeida Silva, I.; Nieto-Muñoz, A. M.; Rodrigues, A. C. M.; Eckert, H. Structure and Lithium-Ion Mobility in $Li_{1.5}M_{0.5}Ge_{1.5}(PO_4)_3$ (M = Ga, Sc, Y) NASICON Glass-Ceramics. *J. Am. Ceram. Soc.* **2020**, *103*, 4002−4012.
(62) Werner-Zwanziger, U.; Paterson, A. L.; Zwanziger, J. W. The Czjzek Distribution in Solid-State NMR: Scaling Properties of Central and Satellite Transitions. *J. Non-Cryst. Solids* **2020**, *550*, No. 120383.
(63) Czjzek, G.; Fink, J.; Götz, F.; Schmidt, H.; Coey, J. M. D.; Rebouillat, J. P.; Liénard, A. Atomic Coordination and the Distribution of Electric Field Gradients in Amorphous Solids. *Phys. Rev. B* **1981**, *23*, 2513.
(64) Massiot, D.; Fayon, F.; Capron, M.; King, I.; Le Calvé, S.; Alonso, B.; Durand, J. O.; Bujoli, B.; Gan, Z.; Hoatson, G. Modelling One- and Two-Dimensional Solid-State NMR Spectra. *Magn. Reson. Chem.* **2002**, *40*, 70−76.
(65) Chopin, L.; Vega, S.; Gullion, T. A MAS NMR Method for Measuring $^{13}C-^{17}O$ Distances. *J. Am. Chem. Soc.* **1998**, *120*, 4406−4409.
(66) van Wüllen, L.; Tricot, G.; Wegner, S. An Advanced NMR Protocol for the Structural Characterization of Aluminophosphate Glasses. *Solid State Nucl. Magn. Reson.* **2007**, *32*, 44−52.
(67) Bak, M.; Rasmussen, J. T.; Nielsen, N. C. SIMPSON: A General Simulation Program for Solid-State NMR Spectroscopy. *J. Magn. Reson.* **2000**, *147*, 296−330.
(68) Barsoukov, E.; Macdonald, J. R. *Impedance Spectroscopy: Theory, Experiment, and Applications*, 2nd ed.; Wiley: Hoboken, 2005.
(69) Fajans, K.; Kreidl, N. J. Stability of Lead Glasses and Polarization of Ions. *J. Am. Ceram. Soc.* **1948**, *31*, 105−114.
(70) Chen, Q.; Ma, Q.; Wang, H.; Wang, Q.; Hao, Y.; Chen, Q. Properties and Structure of Faraday Rotating Glasses for Magneto Optical Current Transducer. *Bol. Soc. Esp. Ceram. Vidrio* **2017**, *56*, 1−12.
(71) Doremus, R. D. *Glass Science*, 2nd ed.; Wiley: New York, 1994.
(72) Meesala, Y.; Chen, C. Y.; Jena, A.; Liao, Y. K.; Hu, S. F.; Chang, H.; Liu, R. S. All-Solid-State Li-Ion Battery Using $Li_{1.5}Al_{0.5}Ge_{1.5}(PO_4)_3$ As Electrolyte Without Polymer Interfacial Adhesion. *J. Phys. Chem. C* **2018**, *122*, 14383−14389.
(73) Wu, X. L.; Zong, J.; Xu, H.; Wang, W.; Liu, X. J. Effects of LAGP Electrolyte on Suppressing Polysulfide Shuttling in Li-S Cells. *RSC Adv.* **2016**, *6*, 57346−57356.
(74) Chen, H.; Tao, H.; Wu, Q.; Zhao, X. Thermal Behavior and Lithium Ion Conductivity of Li_2O-Al_2O_3-TiO_2-SiO_2-P_2O_5 Glass-Ceramics. *J. Wuhan Univ. Technol., Mater. Sci. Ed.* **2012**, *27*, 67−72.
(75) Leo, C. J.; Chowdari, B. V. R.; Rao, G. V. S.; Souquet, J. L. Lithium Conducting Glass Ceramic with Nasicon Structure. *Mater. Res. Bull.* **2002**, *37*, 1419−1430.

https://doi.org/10.1021/acs.jpcc.3c00476
J. Phys. Chem. C 2023, 127, 6207−6225

(76) Xie, H.; Goodenough, J. B.; Li, Y. $Li_{1.2}Zr_{1.9}Ca_{0.1}(PO_4)_3$, a Room-Temperature Li-Ion Solid Electrolyte. *J. Power Sources* **2011**, *196*, 7760−7762.
(77) Chen, D.; Yang, J.; Zhou, Y.; Xie, H.; Zhang, H.; Lai, H. Divalent-Doped $Li_{1.3}Al_{0.3}Ti_{1.7}(PO_4)_3$ Ceramics with Enhanced Microwave Absorption Properties in the X-Band. *J. Electron. Mater.* **2022**, *51*, 2663−2672.
(78) Patnaik, P. *Handbook of Inorganic Chemicals*, 1st ed.; The McGraw-Hill Companies: New York, 2002.
(79) Pramanik, K.; Sau, K.; Kumar, P. P. Role of Framework Flexibility in Ion Transport: A Molecular Dynamics Study of $LiM_2^{IV}(PO_4)_3$. *J. Phys. Chem. C* **2020**, *124*, 4001−4009.
(80) Zuxiang, L.; Huijun, Y.; Shichun, L.; Shunbao, T. Phase Relationship and Electrical Conductivity of $Li_{1+x}Ti_{2-x}Ga_xP_3O_{12}$ and $Li_{1+2x}Ti_{2-x}Mg_xP_3O_{12}$ Systems. *Solid State Ionics* **1986**, *18*−*19*, 549−552.
(81) Shannon, R. D. Revised Effective Ionic Radii and Systematic Studies of Interatomic Distances in Halides and Chalcogenides. *Acta Crystallogr., Sect. A* **1976**, *32*, 751−767.
(82) Tarte, P.; Rulmont, A.; Merckaert-Ansay, C. Vibrational Spectrum of Nasicon-like, Rhombohedral Orthophosphates $M^IM_2^{IV}(PO_4)_3$. *Spectrochim. Acta, Part A* **1986**, *42*, 1009−1016.
(83) Galleani, G.; Santagneli, S. H.; Messaddeq, Y.; De Oliveira, M.; Eckert, H. Rare-Earth Doped Fluoride Phosphate Glasses: Structural Foundations of Their Luminescence Properties. *Phys. Chem. Chem. Phys.* **2017**, *19*, 21612−21624.
(84) Nyquist, R.; Kagel, R. *Handbook of Infrared and Raman Spectra of Inorganic Compounds and Organic Salts*, 1st ed.; Academic Press: New York, 1971.
(85) Nakamoto, K. *Infrared and Raman Spectra of Inorganic and Coordination Compounds: Part A: Theory and Applications in Inorganic Chemistry*, 6th ed.; Wiley: Hoboken, 2009.
(86) He, Q.; Wang, P.; Sun, M.; Lu, M.; Peng, B. Effects of Doping B_2O_3 on the Defects-State in SiO_2-Containing Phosphate Based Glasses. *Opt. Mater. Express* **2017**, *7*, 2697.
(87) Foroutan, F.; de Leeuw, N. H.; Martin, R. A.; Palmer, G.; Owens, G. J.; Kim, H.-W.; Knowles, J. C. Novel Sol-Gel Preparation of $(P_2O_5)_{0.4}$-$(CaO)_{0.25}$-$(Na_2O)_X(TiO_2)_{(0.35-X)}$ Bioresorbable Glasses (X = 0.05, 0.1, and 0.15). *J. Sol−Gel Sci. Technol.* **2015**, *73*, 434−442.
(88) Tsuchida, J. E.; Schneider, J.; Pizani, P. S.; Oliveira, S. L. Lead and Aluminum Bonding in Pb-Al Metaphosphate Glasses. *Inorg. Chem.* **2008**, *47*, 690−698.
(89) Tricot, G. Mixed Network Phosphate Glasses: Seeing Beyond the 1D ^{31}P MAS-NMR Spectra With 2D $^{X/31}P$ NMR Correlation Maps. *Annual Reports on NMR Spectroscopy*, 1st ed.; Academic Press: London, U.K., 2019; Vol. *96*, pp 35−75.
(90) Behrends, F.; Eckert, H. Mixed Network Former Effects in Oxide Glasses: Spectroscopic Studies in the System $(M_2O)_{1/3}[(Ge_2O_4)_x(P_2O_5)_{1-x}]_{2/3}$. *J. Phys. Chem. C* **2014**, *118*, 10271−10283.
(91) d'Espinose de Lacaillerie, J. B.; Fretigny, C.; Massiot, D. MAS NMR Spectra of Quadrupolar Nuclei in Disordered Solids: The Czjzek Model. *J. Magn. Reson.* **2008**, *192*, 244−251.
(92) Galleani, G.; Santagneli, S. H.; Ledemi, Y.; Messaddeq, Y.; Janka, O.; Pöttgen, R.; Eckert, H. Ultraviolet Upconversion Luminescence in a Highly Transparent Triply-Doped Gd^{3+}-Tm^{3+}-Yb^{3+} Fluoride-Phosphate Glasses. *J. Phys. Chem. C* **2018**, *122*, 2275−2284.
(93) Gleizes, A. N.; Samélor, D.; Vahlas, C.; Sarou-Kanian, V.; Florian, P.; Massiot, D. Temperature Dependent 4-, 5- and 6-Fold Coordination of Aluminum in MOCVD-Grown Amorphous Alumina Films: From Local Coordination to Material Properties. *Adv. Sci. Technol.* **2014**, *91*, 123−133.
(94) Edén, M.Update on ^{27}Al NMR Studies of Aluminosilicate Glasses. *Annual Reports on NMR Spectroscopy*; Elsevier B.V., 2020; Vol. *101*, pp 285−410.
(95) Bennett, J. M.; Cohen, J. M.; Artioli, G.; Pluth, J. J.; Smith, J. V. Crystal Structure of $AlPO_4$-21, a Framework Aluminophosphate Containing Tetrahedral Phosphorus and Both Tetrahedral and Trigonal-Bipyramidal Aluminum in 3-, 4-, 5-, and 8-Rings. *Inorg. Chem.* **1985**, *24*, 188−193.
(96) Rodrigues, A. M.; Narváez-Semanate, J. L.; Cabral, A. A.; Rodrigues, A. C. M. Determination of Crystallization Kinetics Parameters of a $Li_{1.5}Al_{0.5}Ge_{1.5}(PO_4)_3$ (LAGP) Glass by Differential Scanning Calorimetry. *Mater. Res.* **2013**, *16*, 811−816.
(97) Sinclair, D. C.; West, A. R. Impedance and Modulus Spectroscopy of Semiconducting $BaTiO_3$ Showing Positive Temperature Coefficient of Resistance. *J. Appl. Phys.* **1989**, *66*, 3850.
(98) Irvine, J. T. S.; Sinclair, D. C.; West, A. R. Electroceramics: Characterization by Impedance Spectroscopy. *Adv. Mater.* **1990**, *2*, 132−138.
(99) Thokchom, J. S.; Kumar, B. Composite Effect in Superionically Conducting Lithium Aluminium Germanium Phosphate Based Glass-Ceramic. *J. Power Sources* **2008**, *185*, 480−485.
(100) Zhu, Y.; Zhang, Y.; Lu, L. Influence of Crystallization Temperature on Ionic Conductivity of Lithium Aluminum Germanium Phosphate Glass-Ceramic. *J. Power Sources* **2015**, *290*, 123−129.
(101) Illbeigi, M.; Fazlali, A.; Kazazi, M.; Mohammadi, A. H. Ionic Conduction and Crystal Structure of Aluminum Doped NASICON-Type $LiGe_2(PO_4)_3$ Glass-Ceramic Crystallized at Different Times and Temperatures. *J. Electroceram.* **2018**, *40*, 180−189.
(102) Narváez-Semanate, J. L.; Rodrigues, A. C. M. Microstructure and Ionic Conductivity of $Li_{1+x}Al_xTi_{2-x}(PO_4)_3$ NASICON Glass-Ceramics. *Solid State Ionics* **2010**, *181*, 1197−1204.

https://doi.org/10.1021/acs.jpcc.3c00476
J. Phys. Chem. C 2023, 127, 6207−6225